Pathway analysis of super-exchange electronic couplings in electron transfer reactions using a multi-configuration self-consistent field method

AUTHOR(S):

Nishioka, Hirotaka; Ando, Koji

Pathway analysis of super-exchange electronic couplings in electron transfer reactions using a multi-configuration self-consistent field method†

Hirotaka Nishioka*[a] and Koji Ando[a]

We present a novel pathway analysis of super-exchange electronic couplings in electron transfer reactions using localized molecular orbitals from multi-configuration self-consistent field (MCSCF) calculations. In our analysis, the electronic coupling and the tunneling pathways can be calculated in terms of the configuration interaction (CI) Hamiltonian matrix obtained from the localized MCSCF wave function. Making use of the occupation restricted multiple active spaces (ORMAS) method can effectively produce the donor, acceptor, and intermediate configuration state functions (CSFs) and CIs among these CSFs. In order to express the electronic coupling as a sum of individual tunneling pathways contributions, we employed two perturbative methods: Löwdin projection-iteration method and higher-order super-exchange method. We applied them to anion couplings of butane-1,4-diyl and pentane-1,5-diyl. The results were (1) the electronic couplings calculated from the two perturbative methods were in reasonable agreement with those from a non-perturbative method (one-half value of the energy difference between the ground and first excited states), (2) the main tunneling pathways consisted of a small number of lower-order super-exchange pathways where bonding, anti-bonding, or extra-valence-shell orbitals were used once or twice, and (3) the interference among a huge number of higher-order super-exchange pathways significantly contributed to the overall electronic coupling, whereas each of them contributed only fractionally. Our method can adequately take into account both effects of non-dynamical electron correlation and orbital relaxation. Comparing with analyses based on the Koopmans' theorem (ignoring both effects) and the ORMAS-CIs from frozen localized reference orbitals (ignoring the effect of orbital relaxation), we discuss these effects.

1 Introduction

The electron transfer (ET) reaction is one of the most fundamental phenomena in chemical, physical, and biological systems and thus has received considerable attention from various scientific fields[1–4]. Among them, the ET reactions between local donor (D) and acceptor (A) groups linked by organic spacer molecules (bridge, B) have been thoroughly investigated experimentally.[5–10] Such ET reactions occur in the non-adiabatic limit and the rate of reaction is given by the following formula:[1–4]

$$k_{DA} = \frac{2\pi}{\hbar}|T_{DA}|^2\,(\mathrm{FCWD})\,, \qquad (1)$$

where (FCWD) is the Franck-Condon weighted density of states and T_{DA} is the electronic coupling between localized donor and acceptor states. In such an ET system linked by spacer molecules, T_{DA} is usually discussed by the following two terms: (1) through-space coupling arising from the direct mixing of the localized donor and acceptor orbitals and (2) through-bond coupling arising from the super-exchange mechanism where the electron tunnels *via* the virtual states of the spacer molecules.[11,12]. The amplitude of T_{DA} is determined by the sum of the two terms. For long-range ET reactions, the through-space coupling is often negligible since the overlap between the donor and acceptor orbitals at a distance greater than several angstroms is extremely small. For this reason, the through-bond coupling mostly contributes to the T_{DA} and as a result, regulates the long-range ET rate.

The theoretical estimation of T_{DA} from the electronic structure of the ET system, especially focusing on the chemical and structural features of the spacer molecules, is a challenging and attractive subject. Many methods based on empirical, semi-empirical and *ab initio* electronic structure calculations have been developed to obtain T_{DA} for various ET systems.[11–19] For long-range ET reactions in DBA systems, only the two effective diabatic states (*i.e.* the charge-localized initial and final diabatic states with exponentially small charge density in the B region) are involved in the electronic coupling, and the electron tunneling occurs when the two diabatic states are brought into resonance by the thermal fluctuation of molecular environment. Under this situation, various *ab initio*-based methods have been applied to calculate the T_{DA}-value in terms of the off-diagonal matrix element between the two diabatic states[17–37] and the half energy difference (energy splitting) between the corresponding two adiabatic states.[17–19,38–46] Furthermore, the Hartree-Fock (HF) Koopmans' theorem (KT) scheme is used to approximate the T_{DA}-value from the half energy splitting between the two corresponding HF molecular orbitals (MOs).[17–19] The *ab initio*-based HF-KT scheme has been widely used for organic[17–19,27,38–40] and biological[47,48] ET systems because of its simplicity and computational efficiency.

In addition to calculating the T_{DA}-values, determining and visualizing the electron tunneling pathways has been a significant subject to understand the role of spacer molecules. Such pathway studies enable us to elucidate the nature of through-bond coupling and have great potential to design effective long-range ET systems for molecular devices. So far, many theoretical pathway analysis methods have also been developed and used[11,16–18,36,37,49–75]. For *ab initio*-MO based path-

[a]*Department of Chemistry, Graduate School of Science, Kyoto University, Sakyo-ku, Kyoto 606-8502, Japan. Fax: +81-75-753-4018; Tel: +81-75-753-4020; E-mail: nishioka@kuchem.kyoto-u.ac.jp*

† Electronic Supplementary Information (ESI) available: Localized ORMAS-MCSCF active orbitals, dependence of $T_{DA}^{p\mathrm{th}}$ and T_{DA} on the energy threshold, dependence of T_{DA} on the number of perturbative terms, dependence of $H_{D,A}^{\mathrm{eff}}$ and T_{DA} on E_{tun}, the main tunneling pathways, and the NBOs used for ORMAS-CI calculations.

way analysis, the HF-KT scheme with natural bond orbitals (NBOs)[76,77] has been most commonly used.[12,17,18,50–57] In these studies, the T_{DA}-values are approximated as the sum of the couplings from individual tunneling pathways obtained by perturbative approaches such as the super-exchange method[49] with the NBO Fock matrix. However, the HF-KT scheme intrinsically ignores the effects of non-dynamical electron correlation and orbital relaxation. Moreover, the quality of the antibonding and Rydberg NBOs are not necessarily much higher than the HF virtual orbitals.

A few of *ab initio*-MO based pathway studies beyond the HF-KT level have been conducted.[36,37,58] Hayashi and Kato[58] have analyzed the super-exchange tunneling pathways for porphyrin-benzoquinone D/A groups linked by organic spacer molecules using a singly excited configuration interaction (CIS) Hamiltonian matrix with localized orbitals. They thus used the HF virtual orbitals and ignored most of the non-dynamical correlations. Stuchebrukhov[36,37] have developed the tunneling currents method that yields the tunneling pathways as spatial distributions of quantum mechanical flux of probability density. Their method does not need virtual orbitals and partially includes the non-dynamical correlations with use of the superposition of two charge-localized diabatic states obtained from the symmetry-broken unrestricted HF (UHF) solutions biorthogonalized by the corresponding orbital transformation.

In this paper, we present a novel pathway analysis using multi-configuration self-consistent field (MCSCF) calculations with orbital localization schemes. The electronic coupling is obtained from the CI Hamiltonian matrix where the configuration state functions (CSFs) are constructed from the optimized and localized active orbitals of the MCSCF wave functions. In particular, we made use of the occupation restricted multiple active spaces (ORMAS) method[78] implemented in the GAMESS program[79] to effectively generate the CI Hamiltonian matrix. For orbital localization, three different orbital-localization schemes, Edmiston-Ruedenberg[80], Foster-Boys[81], Pipek-Mezey[82], implemented in the GAMESS program were used. For the pathway analyses, we employed two perturbative methods: the Löwdin projection-iteration[83,84] method and the higher-order super-exchange method[49]. The tunneling pathways from our method include both the effects of non-dynamical electron correlation and orbital relaxation in contrast to the previous studies. We have applied our method to anion couplings of butane-1,4-diyl and pentane-1,5-diyl where the excess electron is exchanged between the terminal CH_2 π DA groups through alkyl chains. These model ET systems have been studied in many theoretical works owing to their relavance to the ET kinetics in alkane-thiols self-assembled monolayers attached to gold electrodes[85–87]. To clarify the effects of non-dynamical correlation and orbital relaxation, we have also carried out calculations using the NBO Fock matrix (ignoring both effects) and using the ORMAS-CI Hamiltonian matrix constructed with the frozen NBOs (ignoring the orbital relaxation).

The influence of structural fluctuations on the ET electronic couplings are becoming recognized to be of great importance for making quantitative predictions in systems with multiple interfering pathways.[88,89] For biological ET systems, a few of theoretical methods to determine and visualize the tunneling pathways that take into account both the effects of structure fluctuations and quantum-interference among the multiple-tunneling pathways have been developed.[71,72] However, we will leave this interesting issue for future investigations.

The constitution of this paper is as follows: In section 2, we describe the computational method to construct the CI Hamiltonian matrix used for the pathway analyses. We first show the structures of butane-1,4-diyl and pentane-1,5-diyl and then present the method of the ORMAS-MCSCF calculations with the orbital localization schemes for producing CIs. In section 3, we briefly review the Löwdin projection-iteration method and the higher-order super-exchange method for the pathway analyses. In section 4, we present the numerical results of the electronic couplings and the pathway analyses. In section 5, we present the pathway analyses from the NBO Fock matrix and from the ORMAS-CI Hamiltonian matrix with the NBO. In section 6 we conclude.

2 Computational Method

2.1 Structures

The structures of butane-1,4-diyl and pentane-1,5-diyl used in this study are shown in Fig. 1. The coordinates of both molecules were determined by geometrical optimizations in their neutral triplet states with restricted open-shell HF(ROHF)-B3LYP/6-311+G(d).[90] In the geometrical optimizations, the structures of butane-1,4-diyl and pentane-1,5-diyl were constrained to have C_{2h} and C_{2v} symmetries, respectively. To examine the π couplings between the terminal carbon lone-pairs, in the geometrical optimizations, the hydrogen atoms of the terminal CH_2 were also constrained to be perpendicular to the σ_h plane and the σ_v plane, respectively. In adopting these procedures, we followed the previous works[19,46,53] to make comparisons. The use of neutral triplet state is a convenient way to obtain symmetric structures that mimic the transition state of the ET. The uncertainty involved in this approximation is again an interesting issue in relation to the coupling to the structural fluctuation, but we shall leave it out of the scope of this paper. As shown in Fig. 1, we have numbered the carbon atoms of hydrocarbon chain, starting from one terminal carbon atom to the other.

2.2 Electronic Structure Calculations

In the two-state approximation, the $|T_{DA}|$-value is obtained from the half energy difference, $\Delta/2$, between the ground and first excited states[17–19]:

$$|T_{DA}| = \Delta/2 = (E^1 - E^0)/2, \tag{2}$$

where E^0 and E^1 represent the energies of the ground and first excited states, respectively.

To take into account both the effects of non-dynamical electron correlation and orbital relaxation, the MCSCF calculations with orbital localizations schemes were conducted. The procedure of our calculations are as follows: (1) The state-averaged MCSCF (SA-MCSCF) calculations with the occupation restricted multiple active spaces (ORMAS)[78] were conducted for the anion radical ground and first excited states.

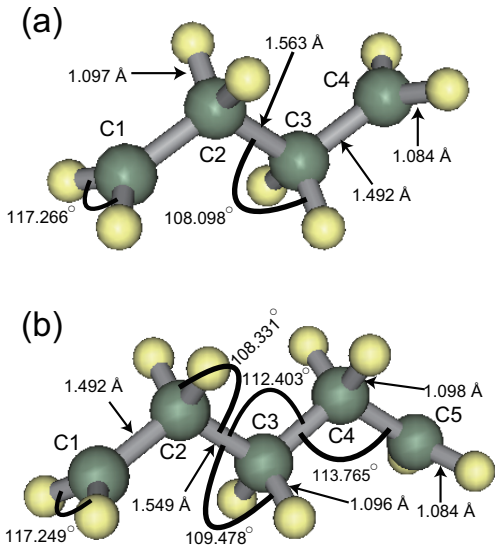

Fig. 1 Structures of (a) butane-1,4-diyl and (b) pentane-1,5-diyl optimized at the neutral triplet state by using ROHF-B3LYP/6-311+G(d). The green and white balls indicate carbon atoms and hydrogen atoms, respectively. We have numbered the carbon atoms of the hydrocarbon chain, starting from one terminal carbon atom to the other. The atomic view is produced with use of Winmostar [108]

The detail of the ORMAS setup will be described later in this subsection. The values of $\Delta/2$ were calculated using eqn 2. (2) After convergence of the ORMAS-MCSCF calculations, the active orbitals were localized with the conventional schemes described later. (3) The ORMAS-CI calculations were redone in the same manner as in step (1) with the localized active orbitals. The CI Hamiltonian matrix elements among the electronic configurations constructed in this step were stored for the pathway analyses. We checked that the value of $\Delta/2$ obtained in this step was identical to that obtained in step (1).

The ORMAS-setup used for steps (1) and (3) is as follows: The active MOs were divided into two groups, (a) ORMAS active orbital group 1 consisting of the doubly and singly occupied MOs in the reference determinant, excluding the frozen core MOs and (b) ORMAS active orbital group 2 consisting of unoccupied MOs up to the number of anti-bonding orbitals in the reference determinant. All excitations within the group 1, and zero or one electron excitations from group 1 to group 2 are taken into account. Schematic representation of this ORMAS setup is shown in Fig. 2(a). The four lowest initial MOs of the ORMAS-MCSCF calculations in step (1) were treated as the frozen core orbitals for butane-1,4-diyl. Similarly, the five lowest initial MOs of the ORMAS-MCSCF calculations in step (1) were frozen for pentane-1,5-diyl. For butane-1,4-diyl, 25 electrons are distributed in 24 active orbitals, giving rise to a total of 2730 determinants. For pentane-1,5-diyl, 31 electrons are distributed in 30 active orbitals, giving rise to a total of 5280 determinants. The assignment of different orbitals in these ORMAS-MCSCF calculations are also illustrated in Fig. 2(a).

In step (2), three different orbital localization schemes were employed, Edmiston-Ruedenberg (Ruedenberg) [80], Foster-Boys (Boys) [81], and Pipek-Mezey (Pop) [82]. To keep the total wave function invariant, these localizations were restricted such that the multiple active spaces were not mixed. The aims of using these localization schemes are to transform the originally delocalized MOs of groups 1 and 2 into localized bonding, lone-pair, and anti-bonding orbitals.

Fig. 2(b) and 2(c) shows the schematic illustrations of the electronic configurations reconstructed in step (3). They include the donor electronic state $|\Phi_D\rangle$, the acceptor electronic state $|\Phi_A\rangle$, and the six types of intermediate electronic states adopted in the pathway analyses. In these electronic configurations, the electrons are distributed into the localized MOs from ORMAS-MCSCF calculations. The CI Hamiltonian matrix elements among these configurations were calculated from the Slater-Condon rules [91] in step (3).

In ORMAS-MCSCF calculations, a determinant-based CI method is employed. [78] The Slater determinants corresponding to $|\Phi_D\rangle$, $|\Phi_A\rangle$, and types I, V, and VI of intermediate electronic states are purely doublets. On the other hand, the Slater determinants corresponding to the types II, III, and IV are not purely doublets owing to spin-contaminations of quartets. To use the CI Hamiltonian matrix elements for the pathway analyses with the higher-order super-exchange method, we should construct the doublet configuration state functions (CSFs) by properly taking linear combinations of the Slater determinants for types II, III, and IV [92]. Note that the Slater determinants are expressed in terms of alpha and beta strings in the determinant-based CI methods. [78,92] Therefore, we should be cautious about the order of such alpha and beta strings when taking the linear combinations to construct the corresponding CSFs. These procedures produce 1872 CSFs for butane-1,4-diyl anion and 3600 CSFs for pentane-1,5-diyl anion, respectively. We confirmed that the $\Delta/2$ values calculated from eqn 2 are invariant using the CSFs.

All electronic structure calculations, including geometrical optimization for the two molecules, were performed using the GAMESS program [79].

3 Theoretical Methods for Pathways Analysis

In this study, two different types of perturbative methods, (1) Löwdin projection-iteration method [83,84] and (2) higher order super-exchange method [18,49], were used to calculate the T_{DA}-value and the tunneling pathways in terms of the CI Hamiltonian matrix obtained from the localized MCSCF wave function. First, we briefly review the theoretical formula of the Löwdin projection-iteration method. This method has been widely used to approximate Δ of the long-range ET in the context of the one-electron models, such as the extended-Hückel level [13,14,93] and the HF-KT level with semi-empirical and *ab initio* MO theories [94–96], except for Ref. [97] in which a Hubbard-like Hamiltonian was used. In contrast, we have used this method in the context of many-electron models based on the CI Hamiltonian matrix.

The system Hamiltonian $\hat{H}$ is written as

$$\hat{H} = \sum_J \sum_K |\Phi_J\rangle H_{J,K} \langle \Phi_K|, \tag{3}$$

where $|\Phi_J\rangle$ represents the CSFs of the donor, acceptor, and the six types illustrated in Fig. 2(b) and 2(c). The diagonal and off-diagonal matrix elements, $H_{J,K}$, are the energies of these

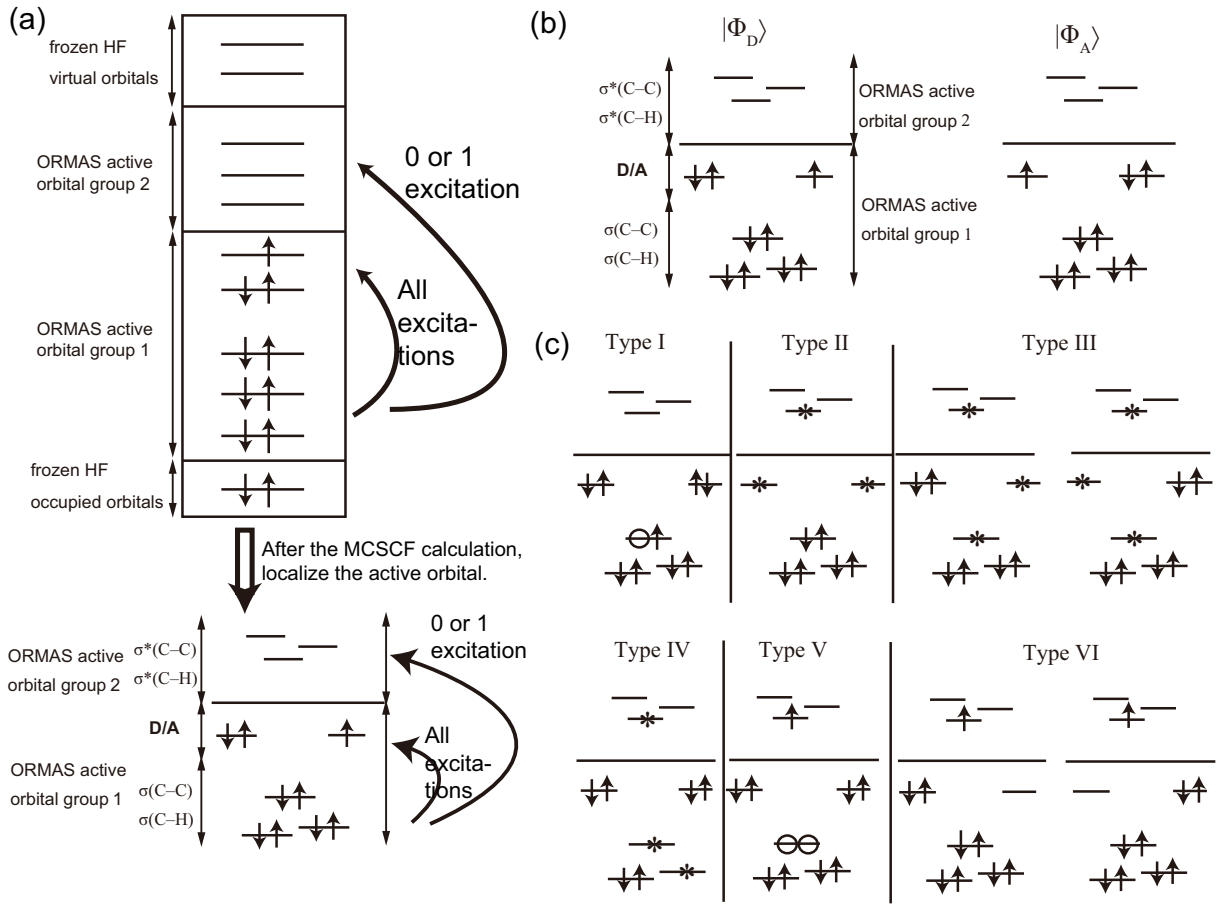

Fig. 2 (a) Schematic representation of the partition of different orbitals used in our ORMAS-MCSCF and ORMAS-CI calculations. (b) Schematic illustrations of the donor and acceptor electronic configurations. The electrons are distributed into the localized MOs from the ORMAS-MCSCF calculation. In an ideal situation, all CC and CH bonding orbitals are occupied doubly, one terminal carbon lone-pair is occupied doubly, and the other terminal carbon lone-pair is occupied singly. (c) Schematic illustrations of the intermediate electronic states used for the super-exchange electronic coupling. The asterisk symbols ∗'s appearing in types of II , III, and IV represent that two up-spin electrons and one down-spin electron occupy each of three MOs singly.

CSFs and the CIs among the corresponding CSFs, respectively. The frozen core energy and nuclear repulsion energy were eliminated in the Hamiltonian matrix elements. Here, we divide the considered CI space into the two subspaces P and Q using the projection operators $\hat{P} = |\Phi_D\rangle\langle\Phi_D| + |\Phi_A\rangle\langle\Phi_A|$ and $\hat{Q} = \sum_J |B_J\rangle\langle B_J|$, where the state $|B_J\rangle$ belongs to the intermediate CSFs as shown in Fig. 2(c). The Löwdin partition of the time-independent Schrödinger equation $\hat{H}|\Psi\rangle = E|\Psi\rangle$ into the subspace P gives the following effective two state Hamiltonian matrix elements [13,15,93,94,96,97]

$$\mathbf{H}^{\mathrm{eff}}_{\mathbf{pp}}(E_{\mathrm{tun}}) = \begin{pmatrix} \mathbf{H}^{\mathrm{eff}}_{D,D}(E_{\mathrm{tun}}) & \mathbf{H}^{\mathrm{eff}}_{D,A}(E_{\mathrm{tun}}) \\ \mathbf{H}^{\mathrm{eff}}_{A,D}(E_{\mathrm{tun}}) & \mathbf{H}^{\mathrm{eff}}_{A,A}(E_{\mathrm{tun}}) \end{pmatrix},$$

$$\mathbf{H}^{\mathrm{eff}}_{P_1,P_2}(E_{\mathrm{tun}}) = E_0\delta_{P_1,P_2} + \sum_J \sum_K \mathbf{V}_{P_1,J}\mathbf{G}^B_{J,K}(E_{\mathrm{tun}})\mathbf{V}_{K,P_2}, \quad (4)$$

where P_1 and P_2 stand for D or A. The matrix $\mathbf{G}^B_{J,K}(E_{\mathrm{tun}})$ is the isolated bridge (*i.e.* intermediate CSF) Green function and E_0 is the average value between the donor and acceptor configuration energies defined as follows:

$$\begin{aligned} \mathbf{G}^B_{J,K}(E_{\mathrm{tun}}) &= \langle B_J|[E_{\mathrm{tun}}\mathbf{I}^B - \mathbf{H}^B]^{-1}|B_K\rangle, & (5) \\ E_0 &= (\langle\Phi_D|\mathbf{H}|\Phi_D\rangle + \langle\Phi_A|\mathbf{H}|\Phi_A\rangle)/2. & (6) \end{aligned}$$

Here, E_{tun} is the parameter that represents the energy of the resonance diabatic states during the electron tunneling transition and is determined by the following iteration procedure. In the first step, the energy E_0 is employed as the initial value of E_{tun}. Then, the effective two-state Hamiltonian is calculated using eqn 4 in which E_{tun} is replaced with E_0. The average value of the diagonal elements of the obtained $\mathbf{H}^{\mathrm{eff}}_{\mathbf{pp}}(E_0)$ is used as the value of E_{tun} in the next step. Therefore, the variable E_n representing the parameter E_{tun} obtained after the n steps of the iteration procedure is written as

$$E_n = (\mathbf{H}^{\mathrm{eff}}_{D,D}(E_{n-1}) + \mathbf{H}^{\mathrm{eff}}_{A,A}(E_{n-1}))/2. \quad (7)$$

The iteration cycle is continued until the value of E_n converges. After the convergence, the approximate electronic coupling and energy gap are obtained as follows:

$$T_{DA} = \mathbf{H}^{\mathrm{eff}}_{D,A}(E_{\mathrm{n-1}}) = \sum_J \sum_K \mathbf{V}_{D,J}\mathbf{G}^B_{J,K}(E_{n-1})\mathbf{V}_{K,A}, \quad (8)$$

$$\begin{aligned} &\Delta^{(2s)}(n)/2 \\ &= \sqrt{\frac{[\mathbf{H}^{\mathrm{eff}}_{D,D}(E_{n-1}) - \mathbf{H}^{\mathrm{eff}}_{A,A}(E_{n-1})]^2}{4} + \mathbf{H}^{\mathrm{eff}}_{D,A}(E_{n-1})\mathbf{H}^{\mathrm{eff}}_{A,D}(E_{n-1})} \\ &= |\mathbf{H}^{\mathrm{eff}}_{D,A}(E_{n-1})|. \end{aligned} \quad (9)$$

Next, we briefly review the theoretical formula of the higher-order super-exchange method [18,49]. This method has been widely used with the NBO method in the context of the one electron models. [12,17,18,50–55] In contrast, we have used this method in the context of the many electron models based on the CI Hamiltonian matrix, similarly to the work by Hayashi and Kato[58]. The system Hamiltonian given by eqn 3 is rewritten as

$$\hat{H} = \hat{H}^0 + \hat{V} = \sum_J |\Phi_J\rangle E_J \langle\Phi_J| + \sum_J \sum_{K(\neq J)} |\Phi_J\rangle V_{J,K}\langle\Phi_K|, \quad (10)$$

where E_J and $V_{J,K}$ are the diagonal and off-diagonal elements of the CI Hamiltonian matrix. The off-diagonal elements, $V_{J,K}$, are regarded as the perturbative terms. In the two state approximation, the approximate electronic coupling is evaluated by using the transition operator formalism of scattering theory [18,49]

$$T_{DA} = \sum_{J,K\notin D,A} \langle\Phi_D|\hat{V}|\Phi_J\rangle\langle\Phi_J|\hat{G}_B(E_{\mathrm{tun}})|\Phi_K\rangle\langle\Phi_K|\hat{V}|\Phi_A\rangle, \quad (11)$$

where $\hat{G}_B$ is the bridge (or intermediated-state) isolated electronic Green function and E_{tun} is the tunneling energy parameter. Employing the Dyson equation, the operator $\hat{G}_B$ is written as follows [18,49]:

$$\begin{aligned} \hat{G}_B(E_{\mathrm{tun}}) &= \hat{G}^0_B(E_{\mathrm{tun}}) + \hat{G}^0_B(E_{\mathrm{tun}})\hat{V}\hat{G}_B(E_{\mathrm{tun}}), & (12) \\ \hat{G}^0_B(E_{\mathrm{tun}}) &= (E_{\mathrm{tun}} - \hat{H}^0 + i\eta)^{-1}, & (13) \end{aligned}$$

where η is a positive infinitesimal constant. The Green function matrix element is therefore written as

$$\begin{aligned} \langle\Phi_J|\hat{G}_B(E_{\mathrm{tun}})|\Phi_K\rangle &= \frac{\delta_{J,K}}{E_{\mathrm{tun}} - E_J} \\ &+ \sum_{L(\neq J)} \frac{1}{E_{\mathrm{tun}} - E_J} V_{J,L}\langle\Phi_L|\hat{G}_B(E_{\mathrm{tun}})|\Phi_K\rangle. \end{aligned} \quad (14)$$

Substituting eqn 14 into eqn 11 provides the approximate electronic coupling as follows:

$$T_{DA} = V_{DA} + \sum_J \frac{V_{D,J}V_{J,A}}{E_{\mathrm{tun}} - E_J} + \sum_J \sum_{K(\neq J)} \frac{V_{D,J}V_{J,K}V_{K,A}}{(E_{\mathrm{tun}} - E_J)(E_{\mathrm{tun}} - E_K)} + \cdots. \quad (15)$$

Equation 15 is rewritten as follows:

$$\begin{aligned} T_{DA} &= \sum_p T^{p\mathrm{th}}_{DA} = T^{1\mathrm{st}}_{DA} + T^{2\mathrm{nd}}_{DA} + T^{3\mathrm{rd}}_{DA} + T^{4\mathrm{th}}_{DA} + \cdots \\ &= \sum_N \beta_N = \beta^{1\mathrm{st}} + \sum_{N_2} \beta^{2\mathrm{nd}}_{N_2} + \sum_{N_3} \beta^{3\mathrm{rd}}_{N_3} + \sum_{N_4} \beta^{4\mathrm{th}}_{N_4} + \cdots, \end{aligned} \quad (16)$$

where β_N represents the electronic coupling propagated by one pathway numbered N. The term $\beta^{p\mathrm{th}}$ represents the electronic coupling provided by the pth-order pathways, where the $(p-1)$ intermediate CSFs are involved. The term $T^{p\mathrm{th}}_{DA}$ represents the contributions from all of the pth-order pathways to the overall electronic coupling. In eqn 15 and 16, the following equalities are obviously satisfied,

$$V_{DA} = T^{1\mathrm{st}}_{DA} = \beta^{1\mathrm{st}} = \langle\Phi_D|\hat{H}|\Phi_A\rangle. \quad (17)$$

When using eqn 15 and 16 in our study, we took into account the pathways providing the coupling whose absolute value was greater than a energy threshold of 10^{-x} hartree, where x was taken from 4 to 10. In addition, when using eqn 15 and 16, we took into account the contributions from up to the 6th-order pathways. The sign of T_{DA} obtained from the higher-order super-exchange method is arbitrary. In the present study, we always took the sign of T_{DA} positively and determined the signs of β_N's and $T^{p\mathrm{th}}_{DA}$ appearing in eqn 16 consistently.

4 Results and Discussion

4.1 Calculated values of $\Delta/2$ employing various basis sets

By using eqn 2 with the ORMAS-MCSCF calculations, we first calculated the $\Delta/2$-values for the anion couplings of butane-1,4-diyl and pentane-1,5-diyl. To compare with the HF-KT scheme[17,39], we also calculated $\Delta/2$ from the half energy splitting between the two highest occupied molecular orbitals (HOMOs) of the ROHF wave function for the neutral triplet and from the half energy splitting between two lowest unoccupied molecular orbitals (LUMOs) for down-spin electrons of the UHF wave function for the neutral triplet. In these calculations, we used several basis sets, including the minimal basis set STO-3G[98], Pople basis sets[99–102] 3-21G, 6-31G, 6-31G(d), 6-311G(d,p), and Dunning 'correlation-consistent' basis sets cc-pVDZ, cc-pVTZ[103]. For the anion coupling of butane-1,4-diyl, the basis sets including diffuse functions, 3-21++G, 6-31+G(d), 6-31++G(d)[104], and aug-cc-pVDZ[103] were also used.

Table 1 Calculated values of the half energy splitting, $\Delta/2$ (in units of millihartree), for anion coupling of butane-1,4-diyl in various basis sets

Basis Set	ORMAS-MCSCF	ROHF-KT	UHF-KT
STO-3G	23.77	19.74	25.06
3-21G	16.45	17.01	14.22
3-21++G	9.714	15.32	3.924
6-31G	14.50	15.78	11.07
6-31G(d)	13.96	15.26	10.60
6-31+G(d)	8.764	13.99	4.599
6-31++G(d)	8.388	14.01	4.472
6-311G(d,p)	12.19	14.53	5.310
cc-pVDZ	12.87	14.80	7.934
aug-cc-pVDZ	8.346	13.92	3.689
cc-pVTZ	11.10	14.20	2.979

In Table 1, we list the results for the anion coupling of butane-1,4-diyl. As shown, the $\Delta/2$-values from the ORMAS-MCSCF calculations were smaller than those from the ROHF-KT calculations and larger than those from the UHF-KT calculations except when the STO-3G basis set was employed. There were more than one millihartree (mh) differences between $\Delta/2$ from the ORMAS-MCSCF calculations and that from the ROHF-KT calculations except when the 3-21G basis set was employed. The value of $\Delta/2$ from any calculations without diffuse functions decreased as we employed larger basis sets. The ORMAS-MCSCF and UHF-KT calculations with the basis sets including diffuse functions decreased the $\Delta/2$-values drastically. Miller *et al.*[39,42] have reported that the HF-KT, ΔSCF, and ΔMP2 calculations with the diffuse-function basis sets produce erratic and unrealistic $\Delta/2$-values for butane-1,4-diyl anion. The reason of these problematic results will be described later in this subsection.

In Table 2, we list the results for the anion coupling of pentane-1,5-diyl. Comparing Table 2 with Table 1 shows that the dependence of the $\Delta/2$-values on the size of the basis set was similar between the two molecules. In contrast to the case for butane-1,4-diyl, the $\Delta/2$-values from the ORMAS-MCSCF calculations were larger than those from the ROHF-KT calculations and smaller than those from the UHF-KT calculations.

Table 2 Calculated values of the half energy splitting, $\Delta/2$ (in units of millihartree), for anion coupling of pentane-1,5-diyl in various basis sets

Basis Set	ORMAS-MCSCF	ROHF-KT	UHF-KT
STO-3G	15.21	12.10	17.27
3-21G	18.38	15.18	21.13
6-31G	17.40	14.54	20.17
6-31G(d)	16.82	14.31	19.67
6-311G(d,p)	16.80	14.19	21.72
cc-pVDZ	16.76	14.28	20.68
cc-pVTZ	15.94	14.04	18.31

To verify the validity of our ORMAS-MCSCF calculations, we recalculated $\Delta/2$ for anion coupling of butane-1,4-diyl adding the ten lowest (previously frozen) virtual orbitals to ORMAS active group 2 and allowing up to two electron excitations from ORMAS active group 1 to group 2. These procedures increased the number of Slater determinants from 2730 to 2440152, and yielded the $\Delta/2$-values of 17.06 mh at 3-21G level, 15.18 mh at 6-31G(d) level, 14.18 mh at cc-pVDZ level, and 10.34 mh at 6-31+G(d) level, respectively. Their agreement with the results in Table 1 except for 6-31+G(d) level indicates that our ORMAS-MCSCF setting described in Section 2 is sufficient for the present analysis without using diffuse-function basis sets.

The choice of the proper size of basis set is of significance for the study on the electronic coupling of ET. Employing larger basis sets does not necessarily produce better results, not only for electronic coupling[38,39,42], but also for response properties[105] and transmission functions[106]. This is explained as follows: (1) HF calculations for anion systems with the diffuse-function basis sets produce the lowest lying virtual orbitals corresponding to the "discrete" continuum states.[38,39,42] They describe unbound electronic states, rather than the chemically relevant virtual MOs, and may lead to erroneous $\Delta/2$-values. (2) Employing improper atom-centered basis sets leads to artifacts due to the "ghost" functions;[39,106] when triple-zeta or bigger basis sets are used, the "ghost" functions may also produce the "discrete" continuum states and cause an artificially high electronic transmission through the alkane molecular junctions.[106] These problems are still open to further investigations. We therefore focus our analysis hereafter on the calculations with the double-zeta basis sets without diffuse functions.

In this study we ignored the dynamical electron correlation because it has been shown to be minor, both qualitatively[20] and by spin-flip (SF) coupled-cluster single and double (CCSD) calculations.[46]

4.2 Active orbital localizations

We localized the active orbitals of the ORMAS-MCSCF wave functions using three different localization schemes, Ruedenberg[80], Boys[81], and Pop[82] with the 3-21G, 6-31G(d), and cc-pVDZ basis sets. In Fig. 3, we show the orbitals localized by the Ruedenberg scheme with the 3-21G basis set for the anion coupling of butane-1,4-diyl. In Fig. 3(a), the localized orbitals in ORMAS active group 2 are drawn. In Fig. 3(b) and 3(c), the localized orbitals in ORMAS active group 1 are

drawn. We have numbered these orbitals as φ_i $(i = 1, \cdots, 24)$, as indicated in Fig. 3. The manner to divide these orbitals corresponds to those in Fig. 2(b) and 2(c). The orbitals drawn in Fig. 3(c) formed the desired bonding orbitals, representing the Lewis-like structure for butane-1,4-diyl. The orbitals drawn in Fig. 3(b) formed the lone-pair orbitals at C1 and C4 and were regarded as the donor φ_D and acceptor φ_A orbitals. Fig. 3(a) shows that most of the orbitals in ORMAS group 2 formed desired anti-bonding ones. Note that the orbitals φ_{17} and φ_{19} in Fig. 3(a) formed extra-valence-shell ones. We hereafter call such orbitals Rydberg orbitals, referring to previous studies[54]. In addition, the orbitals φ_{20} and φ_{22} formed somewhat delocalized three or four center anti-bonding orbitals. In Fig. 3, the symbols 'σ' and 'σ^*' represent bonding and anti-bonding orbitals, respectively. We have named the covalent bonds where the bonding orbitals were located, as written in parentheses in Fig. 3.

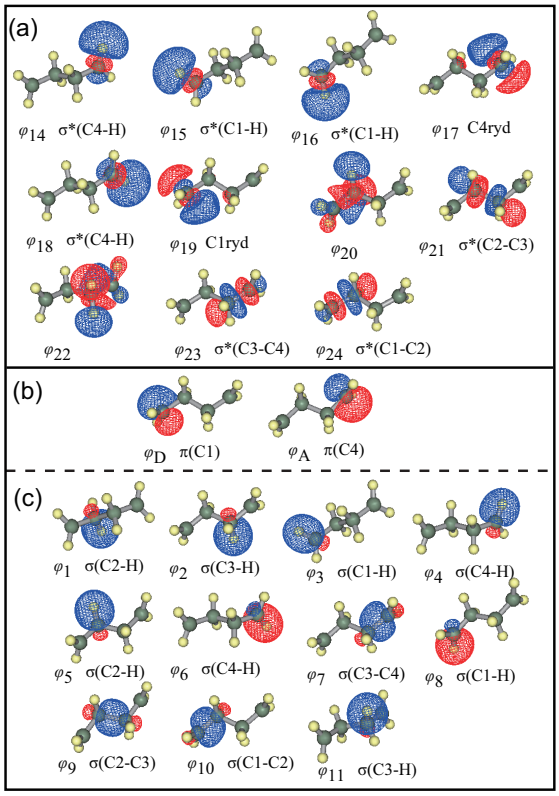

Fig. 3 Localized ORMAS-MCSCF active orbitals obtained with the Ruedenberg localization scheme and the 3-21G basis set for anion coupling of butane-1,4-diyl. (a) The localized active orbitals belonging to the ORMAS active orbital group 2. (b) The localized active orbitals that belong to the ORMAS active orbital group 1 which are regarded as the donor and acceptor orbitals in the pathways analyses. (c) The localized active orbitals belonging to the ORMAS active orbital group 1. These active orbitals were visualized using Winmostar.[108]

When employing the Ruedenberg scheme with the 3-21G basis set for the anion coupling of pentane-1,5-diyl, we found that the localized active orbitals have similar features to those for butane-1,4-diyl. The obtained orbitals in the ORMAS active group 1 formed desired bonding and lone-pair orbitals. The obtained orbitals in the ORMAS active group 2 formed desired anti-bonding orbitals except for the C-H anti-bonding ones located at the spacer alkane $-(CH_2)_3-$ and two Rydberg ones at the terminal carbon atoms. For details, see Fig. S1, ESI.†

For both molecules, the active orbitals obtained with the 6-31G(d) or cc-pVDZ basis set were somewhat less localized than those obtained with 3-21G basis set, not depending on the localization schemes. We also found that the shapes of the localized orbitals from the Boys scheme were closer to those from the Ruedenberg scheme than those from the Pop scheme. For details, see Fig. S2 and S3, ESI.†

These localized MOs constructing the ORMAS-MCSCF wave function were used for the pathway analyses described hereafter in this section.

4.3 Löwdin projection-iteration method

Using the CI Hamiltonian matrix obtained from the localized ORMAS-MCSCF wave functions, we applied the Löwdin projection-iteration method. The initial value for the tunneling energy, E_0, used for this method was the average one between the donor and acceptor CSFs, given by eqn 6.

In Tables 3 and 4, we listed the converged values of $|\mathbf{H}^{\mathrm{eff}}_{D,A}|$ from eqn 8, the ratio $2|\mathbf{H}^{\mathrm{eff}}_{D,A}|/\Delta$, and E_{tun} when using the 3-21G, 6-31G(d), and cc-pVDZ basis sets with the Ruedenberg, Boys, and Pop localization schemes. Tables 3 and 4 show the results for anion couplings of butane-1,4-diyl and pentane-1,5-diyl, respectively. In Tables 3 and 4, we also listed the average value of the configuration energies between the ground and first excited states, $(E^0 + E^1)/2$, obtained from the ORMAS-MCSCF calculations. These configuration energies do not include the frozen core energies and the nuclear repulsion energies to ensure the consistency with the CI Hamiltonian matrix elements used in the Löwdin interaction-projection method. We found that the off-diagonal elements of effective two-state Hamiltonian at the first iteration step (i.e. $|\mathbf{H}^{\mathrm{eff}}_{D,A}(E_0)|$) provide poor approximation of $\Delta/2$ in all cases. For example, when employing the 3-21G basis set and the Ruedenberg localization scheme, we obtained $E_0 = -91.627337$ hartree and $|\mathbf{H}^{\mathrm{eff}}_{D,A}(E_0)| = 324.0$ mh for the anion coupling of butane-1,4-diyl. In this case, the $|\mathbf{H}^{\mathrm{eff}}_{D,A}(E_0)|$-value is thus 19.7 times larger than the $\Delta/2$-value. However, all of these calculations converged quite smoothly within thirty iterative steps, and the converged values of $|\mathbf{H}^{\mathrm{eff}}_{D,A}|$ provided a reasonable approximation of $\Delta/2$, as shown in Tables 3 and 4. The converged values of $|\mathbf{H}^{\mathrm{eff}}_{D,A}|$ obtained from the Boys localization scheme were similar to those obtained from the Ruedenberg localization scheme. As shown in Table 3, the converged values of $|H^{\mathrm{eff}}_{DA}|$ from the Boys and the Ruedenberg schemes were ca. 1.5 times larger than the values of $\Delta/2$ with any of the three basis sets for butane-1,4-diyl. As shown in Table 4, on the other hand, the converged values of $|H^{\mathrm{eff}}_{DA}|$ from these localization schemes are approximately equal to the values of $\Delta/2$ with any of the three basis sets fro pentane-1,5-diyl. In contrast, in the case of the Pop localization scheme, the converged values of $|H^{\mathrm{eff}}_{DA}|$ for anion coupling of butane-1,4-diyl were almost equal to the values of $\Delta/2$, but those for anion coupling of pentane-1,5-diyl were ca. one-third of the values of $\Delta/2$ with any of the three basis sets.

The Löwdin projection-iteration method can take into account the (effectively infinite) higher-order perturbative contributions. Therefore, ideally the results from this method

Table 3 Converged values of the various quantities obtained from the Löwdin projection-iteration method for anion coupling of butane-1,4-diyl

Basis set	Orbital Localization	$\lvert\mathbf{H}^{\mathrm{eff}}_{D,A}(E_{\mathrm{tun}})\rvert$ (mh)	$2\lvert\mathbf{H}^{\mathrm{eff}}_{D,A}(E_{\mathrm{tun}})\rvert/\Delta$ (ratio)	E_{tun} (hartree)	$(E^1+E^0)/2$ (hartree)
3-21G	Boys	24.5	1.49	−91.9372892	−91.9361747
	Ruedenberg	24.8	1.51	−91.9373250	
	Pop	15.7	0.956	−91.9368545	
6-31G(d)	Boys	21.8	1.56	−92.1271099	−92.1262441
	Ruedenberg	21.3	1.53	−92.1270986	
	Pop	14.2	1.02	−92.1267658	
cc-pVDZ	Boys	20.5	1.60	−92.1440432	−92.1432995
	Ruedenberg	20.5	1.59	−92.1440607	
	Pop	13.6	1.06	−92.1437878	

Table 4 Converged values of the various quantities obtained from the Löwdin projection-iteration method for anion coupling of pentane-1,5-diyl

Basis set	Orbital Localization	$\lvert\mathbf{H}^{\mathrm{eff}}_{D,A}(E_{\mathrm{tun}})\rvert$ (mh)	$2\lvert\mathbf{H}^{\mathrm{eff}}_{D,A}(E_{\mathrm{tun}})\rvert/\Delta$ (ratio)	E_{tun} (hartree)	$(E^1+E^0)/2$ (hartree)
3-21G	Boys	18.6	1.01	−128.1690344	−128.1680606
	Ruedenberg	18.3	0.996	−128.1690378	
	Pop	12.0	0.652	−128.1687087	
6-31G(d)	Boys	15.6	0.930	−129.9102720	−129.9094783
	Ruedenberg	15.0	0.889	−129.9102556	
	Pop	10.9	0.648	−129.9100171	
cc-pVDZ	Boys	15.6	0.930	−129.6160627	−129.6152863
	Ruedenberg	15.1	0.902	−129.6160680	
	Pop	10.9	0.652	−129.6158465	

should not depend on the localization schemes in principle. In all cases, the converged values of E_{tun} were highly consistent with the values of $(E^0+E^1)/2$ within ca. 1 mh. On the other hand, $|H^{\mathrm{eff}}_{DA}|$ depended on the localization schemes, as described above. We were unable to resolve satisfactorily clear reason for this, and shall leave it open for future investigations.

4.4 Higher-order super-exchange calculations

Next, we applied the higher-order super-exchange method using the CI Hamiltonian matrix obtained from the localized ORMAS-MCSCF wave function. We employed the three basis sets, 3-21G, 6-31G(d), and cc-pVDZ for this method. We took the E_{tun}-value from the corresponding converged value of E_{tun} from the Löwdin projection-interaction method, listed in Tables 3 and 4.

First, we examined the dependencies of each perturbation term in eqn 16 on the energy threshold. In Fig. 4, we plot the calculated values of $T^{p\mathrm{th}}_{DA}$ and T_{DA} as functions of the energy threshold for butane-1,4-diyl (a) and pentane-1,5-diyl (b). The results in Fig. 4 were obtained using the Ruedenberg localization scheme with the 3-21G basis set. As shown in Fig. 4(a), we obtained a good convergence for all of the perturbative terms $T^{p\mathrm{th}}_{DA}$ (p = 1, ⋯, 6) and T_{DA} with the energy thresholds less than 10^{-8} hartree. Fig. 4(b) shows that a good convergence for up to the 4th-order term was obtained when the energy threshold was less than 10^{-8} hartree. On the other hand, the $T^{5\mathrm{th}}_{DA}$, $T^{6\mathrm{th}}_{DA}$, and T_{DA} still slightly varied as the energy threshold is decreased below 10^{-8} hartree. When using the other basis sets and the other localization schemes, we observed similar good convergence behaviors of $T^{p\mathrm{th}}_{DA}$'s and T_{DA} for butane-1,4-diyl. For pentane-1,5-diyl, we obtained better convergence behaviors from the Pop localization scheme than those from the Ruedenberg or Boys localization scheme. For details, see Fig. S4 and S5, ESI.†

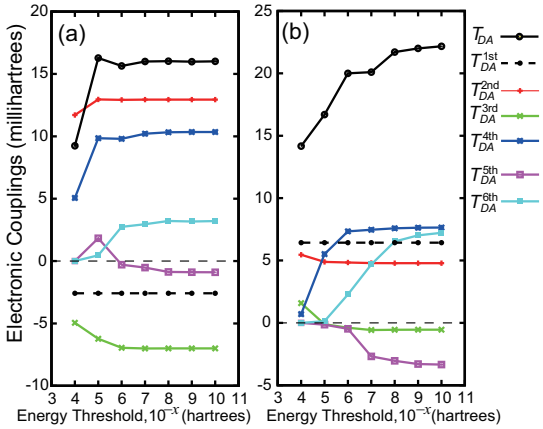

Fig. 4 Dependence of calculated values of perturbative terms $T^{p\mathrm{th}}_{DA}$ in eqn 16 and T_{DA} on the energy threshold for anion couplings of (a) butane-1,4-diyl and (b) pentane-1,5-diyl. The Ruedenberg localization scheme with the 3-21G basis set was used.

In Fig. 5, we plot the total number of pathways as functions of the energy threshold for butane-1,4-diyl (solid) and pentane-1,5-diyl (dashed). The results in Fig. 5 were obtained by using the 3-21G basis set and the Ruedenberg localization scheme, corresponding to the results in Fig. 4. Fig. 5 shows that the total number of pathways followed approximately an

exponential growth with increasing x in the energy threshold 10^{-x} hartree.

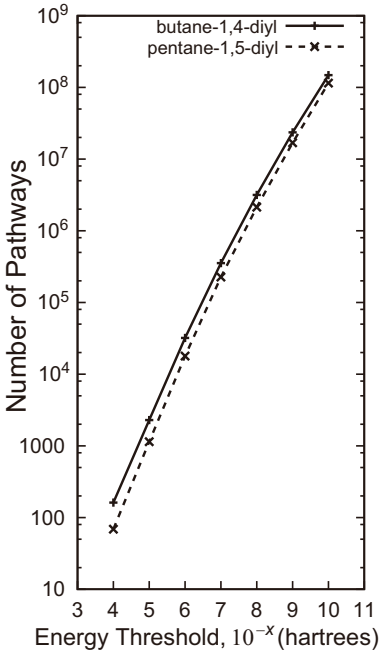

Fig. 5 Dependence of the total number of pathways taken into account in eqn 16 on the energy threshold for anion couplings of (a) butane-1,4-diyl and (b) pentane-1,5-diyl. The Ruedenberg localization scheme with the 3-21G basis set was used. Up to 6th-order pathways providing the coupling whose absolute value was greater than the energy threshold were counted.

Table 5 summarizes the calculated results of $T_{DA}^{p\text{th}}$'s, T_{DA}, and the ratio $2|T_{DA}|/\Delta$ for butane-1,4-diyl with the energy threshold of 10^{-9} hartree. The obtained ratios of $2|T_{DA}|/\Delta$'s were nearly 1 for all the basis sets and orbital localization schemes. These results indicate the validity of the perturbative approach using the higher-order super-exchange method. Table 5 shows that the second-order terms, $|T_{DA}^{2\text{nd}}|$'s provided the largest values among the perturbative terms but the higher-order terms were not so small that they can be ignored. In all cases, the terms $T_{DA}^{2\text{nd}}$'s, $T_{DA}^{4\text{th}}$'s, and $T_{DA}^{6\text{th}}$'s provided the positive values and the terms $T_{DA}^{3\text{rd}}$'s and $T_{DA}^{5\text{th}}$'s provided the negative values. Since the sign of the value of T_{DA} was always taken to be positive, the terms $T_{DA}^{2\text{nd}}$'s, $T_{DA}^{4\text{th}}$'s, and $T_{DA}^{6\text{th}}$'s contributed constructively and the terms $T_{DA}^{3\text{rd}}$'s and $T_{DA}^{5\text{th}}$'s contributed destructively to the overall electronic couplings T_{DA}'s.

Table 6 summarizes the calculated results of $T_{DA}^{p\text{th}}$'s, T_{DA}, and the ratio $2|T_{DA}|/\Delta$ for pentane-1,5-diyl with the energy threshold of 10^{-9} hartree. We did not obtain the obvious patterns about the signs of the terms $T_{DA}^{p\text{th}}$ for pentane-1,5-diyl like the results for butane-1,4-diyl. The ratios of $2|T_{DA}|/\Delta$'s calculated with the Ruedenberg or Boys localization scheme were not as close to unity as those for butane-1,4-diyl because the higher-order perturbative terms did not converge thoroughly in the range of the energy threshold we used (See Fig. 4(b) and S5, ESI†). On the other hand, $2|T_{DA}|/\Delta$'s calculated with the Pop localization scheme were very close to unity for all the basis sets, owing to the good convergence of the higher perturbative terms (See Fig. S5, ESI†). The differences in the convergence properties are explained as follows: The localized donor and acceptor orbitals, φ_D and φ_A, obtained from the Pop scheme were less localized than those from the other schemes, leading to an increase in the dominance of the direct term $T_{DA}^{1\text{st}}$ relative to the contributions from the perturbative terms, as seen in Table 6.

In the super-exchange method we took into account up to 6th order pathways, owing mainly to the present computational limitation. To check the convergence, we plotted the T_{DA} from eqn 15 with respect to the number of perturbative terms in Fig. S6, ESI.† Although strict convergence has not been observed, it will be demonstrated in section 4.6 that the pathway decomposition analysis, taking into account up to the $T_{DA}^{6\text{th}}$ terms always produced reasonable results.

It is also an interesting issue to verify how close the energy can be to E_{tun} in the denominator, for instance in eqn 15, for the perturbative methods to fail. In general, when $V_{JK}/(E_{tun}-E_J) \ll 1$, the super-exchange calculation shows the good convergence and produces a reasonable T_{DA}-value. On the other hand, when $V_{JK}/(E_{tun}-E_J)$ approaches to 1, the super-exchange calculation shows poor convergence and produces an unrealistic T_{DA}-value. To demonstrate this issue in our calculations, we studied the dependence of the $H_{D,A}^{\text{eff}}$-value from eqn 8 and the T_{DA}-value from eqn 15 on the E_{tun} for butane-1,4-diyl with the Reudenberg scheme and the 3-21G basis set. The obtained results are shown in Fig. S7, ESI.† We can see that the T_{DA}-value from eqn 15 diverges exponentially from the $\Delta/2$-value as E_{tun} deviates linearly from $\frac{E^1+E^0}{2}$.

The results in Fig. 4 and 5 indicate that the contributions from a huge number of pathways (23581215 for butane-1,4-diyl and 16851785 for pentane-1,5-diyl with the energy threshold of 10^{-9} hartree) determined the converged values of T_{DA}. This demonstrates that complicated interferences among a large number of tunneling pathways are in effect. Since the total number of pathways increased exponentially with increasing x in the energy threshold, 10^{-x} hartree, the good convergences of T_{DA}'s were due to the fact that the contributions from a huge number of pathways providing the coupling $|\beta|$, less than 10^{-8} hartree cancel out.

4.5 Main electron tunneling pathways

In the framework of the super-exchange method based on eqn 16, the pathways providing the large $|\beta|$-values can be regarded as the main ones. As shown in Table 5, the agreement between the perturbative T_{DA} values from eqn 16 with the non-perturbative $\Delta/2$ values from eqn 2 was pretty good for the anion coupling of butane-1,4-diyl. Thus, we focused on its main tunneling pathways.

Fig. 6 schematically illustrates the main pathways obtained using the Ruedenberg localization scheme with the 3-21G basis set. The calculated values of $|\beta|$, $V_{J,K}$, and $(E_{\text{tun}}-E_J)$ (underlined numbers) are also given in Fig. 6. Fig. 6(a) shows the main second-order tunneling pathways involving one intermediate state in CSF type I, where only a "hole" moves through a bonding orbital from φ_A to φ_D as shown in the left side of the figure. These pathways are regarded as the pure "hole" transfer (h-transfer) pathways.[18,55,58] In the right side of Fig. 6(a), we schematically visualize the main second-order h-transfer pathways by the diagrams similar to those used previously.[50–53] We found that the second-order h-

Table 5 Higher-order super-exchange calculations for anion coupling of butane-1,4-diyl with the energy threshold of 10^{-9} hartree

Basis Set	Orbital Localization	T_{DA}^{1st} (mh)	T_{DA}^{2nd} (mh)	T_{DA}^{3rd} (mh)	T_{DA}^{4th} (mh)	T_{DA}^{5th} (mh)	T_{DA}^{6th} (mh)	T_{DA} (mh)	$2\|T_{DA}\|/\Delta$ (ratio)
3-21G	Boys	−2.65	13.6	−8.20	12.0	−2.90	4.85	16.7	1.02
	Ruedenberg	−2.58	12.9	−7.00	10.3	−0.894	3.17	16.0	0.972
	Pop	5.08	11.2	−8.59	10.2	−4.06	4.85	18.6	1.13
6-31G(d)	Boys	−3.26	11.5	−6.54	9.74	−1.61	3.51	13.3	0.954
	Ruedenberg	−2.72	11.1	−6.22	9.13	−0.759	2.55	13.1	0.938
	Pop	3.59	9.69	−7.30	8.60	−3.08	4.00	15.5	1.11
cc-pVDZ	Boys	−3.35	10.8	−6.05	9.19	−1.53	3.25	12.3	0.957
	Ruedenberg	−3.19	10.4	−5.62	8.39	−0.285	2.02	11.7	0.912
	Pop	2.90	8.56	−6.20	7.07	−1.58	2.62	13.4	1.04

Table 6 Higher-order super-exchange calculations for anion coupling of pentane-1,5-diyl with the energy threshold of 10^{-9} hartree

Basis Set	Orbital Localization	T_{DA}^{1st} (mh)	T_{DA}^{2nd} (mh)	T_{DA}^{3rd} (mh)	T_{DA}^{4th} (mh)	T_{DA}^{5th} (mh)	T_{DA}^{6th} (mh)	T_{DA} (mh)	$2\|T_{DA}\|/\Delta$ (ratio)
3-21G	Boys	5.78	5.15	−1.54	9.44	−5.20	9.12	22.8	1.24
	Ruedenberg	6.43	4.78	−0.549	7.63	−3.30	7.01	22.0	1.20
	Pop	11.1	2.55	1.76	1.98	1.78	0.132	19.3	1.05
6-31G(d)	Boys	6.41	0.661	5.76	−1.85	8.79	−8.90	10.9	0.646
	Ruedenberg	7.21	−0.223	6.48	−2.29	8.69	−8.62	11.3	0.669
	Pop	10.3	0.481	3.92	0.0242	2.90	−0.394	17.2	1.03
cc-pVDZ	Boys	6.56	0.183	6.22	−0.962	6.98	−5.82	13.2	0.786
	Ruedenberg	7.17	−0.605	6.79	−1.42	7.16	−5.88	13.2	0.789
	Pop	10.4	−1.01	5.80	−0.895	3.63	−0.788	17.1	1.02

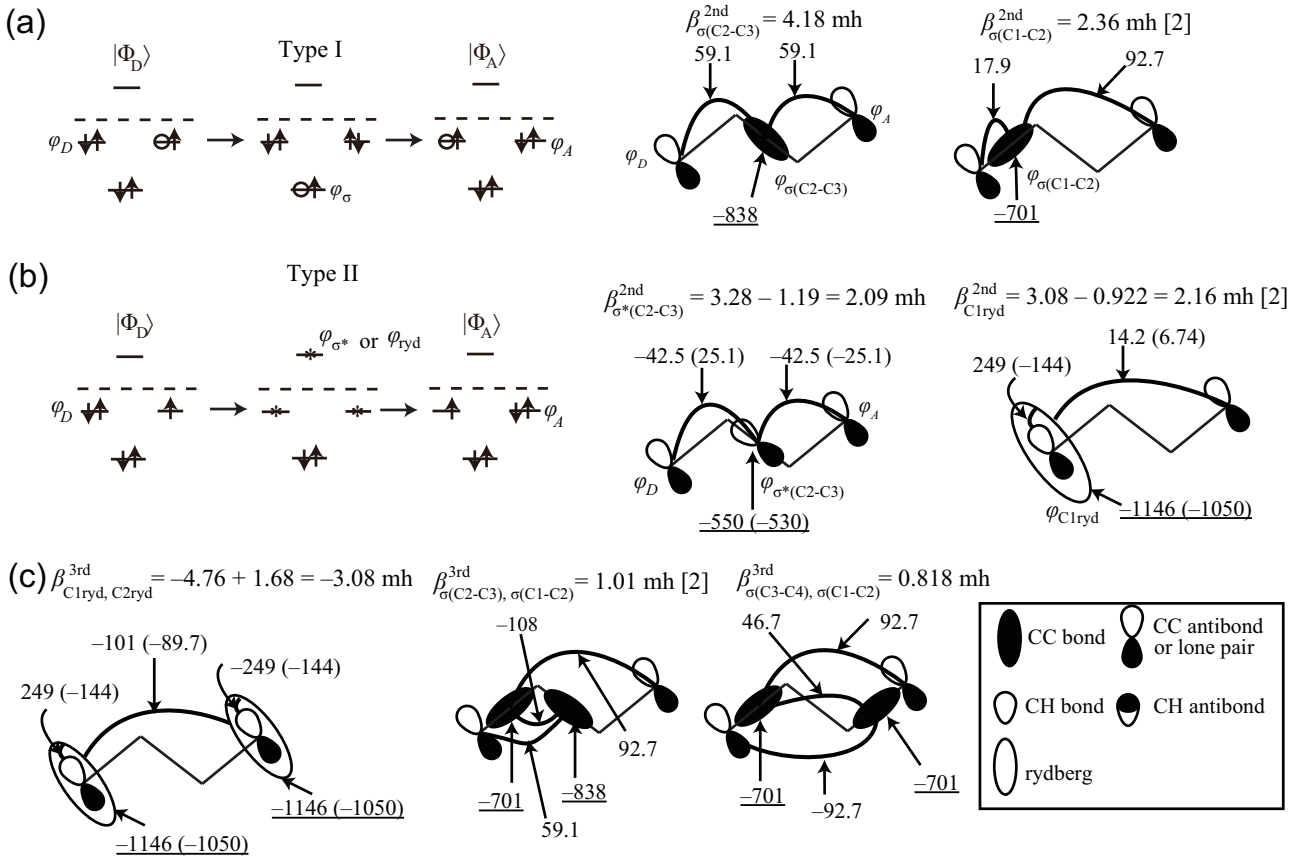

Fig. 6 Main tunneling pathways obtained from the super-exchange method based on the ORMAS-MCSCF calculation for anion coupling of butane-1,4-diyl. The Ruedenberg orbital localization scheme with the 3-21G basis set was used. (a) The h-transfer pathways where a hole moves through the intermediate state in CSF type I once. (b) The e-transfer pathways where an electron moves through the intermediate state in CSF type II once. (c) The third order pathways. The value of coupling β propagated by the corresponding pathway is given in millihartree (mh). The sign convention for the β-values is written in text. Matrix element $V_{J,K}$ and denominators E_J (underlined) appeared in eqn 15 are also given in mh.

transfer pathway through the σ(C2-C3) orbital provided the largest |β|-value (4.18 mh). Owing to the C_{2h} symmetry of butane-1,4-diyl, the second-order h-transfer pathway through the σ(C3-C4) orbital provided the β-value identical with the $\beta^{2nd}_{\sigma(C1-C2)}$. The number of such equivalent pathways due to the symmetry of molecule are given in square brackets in Fig. 6.

In Fig. 6(b), we illustrate the main second-order pathways involving one intermediate state in the CSF type II, where only an "electron" moves through an anti-bonding or Rydberg orbital from φ_D to φ_A. These pathways are regarded as the pure "electron" transfer (e-transfer) pathways.[18,55,58] It should be noticed that for the intermediate states classified into CSF type II there are two CSFs in which the same active orbital in ORMAS active group 2 is occupied by one electron as described in section 3.2. Therefore, there are two second-order e-transfer pathways where an "electron" tunnels through the same anti-bonding or Rydberg orbital. One diagram in Fig. 6(b) represents the two second-order e-transfer pathways involving an "electron" tunneling through the σ*(C2-C3) orbital once; One of the two e-transfer pathways provided 3.28 mh and the other provided −1.19 mh (the values of $V_{J,K}$ and $(E_{\rm tun}-E_J)$ are given in parenthesis). In this study, we treated the two e-transfer pathways together and regarded 2.09 mh as the β-value. The other diagram in Fig. 6(b) represents the main second-order e-transfer pathways involving a long-distance "electron" tunneling through the Rydberg orbital at C1 or C4 atom once.

As shown in Fig. 6, the obtained main third-order pathways were only the h-transfer and e-transfer pathways. The β-values provided by each of the main h-transfer pathways were almost comparable with those by each of the main e-transfer pathways. In these pathways, the "hole/electron" skips the adjacent covalent bond/anti-bond, in contrast with simple McConnell's picture[11] that predicts the "hole/electron" moves along a sequence of the nearest-neighbor covalent link. For example, the two third-order h-transfer pathways in Fig. 6(c) exhibited that a "hole" first transfers from φ_A to the non-adjacent C-C bonding orbital, then goes backward, passes through the C-C bonding orbital distant from φ_D, and lastly reaches φ_D. These pathways are attributed to the small $V_{J,K}$-values arising from small overlap between φ_D/φ_A and the adjacent σ(C-C) orbital (see Fig. 6(a)).

In the case of the other localization schemes or the other basis sets, we obtained similar main tunneling pathways. For details, see Fig. S8 - S10, ESI.†

4.6 Decomposition of T_{DA} into sum of contributions from intermediate CSF types

As shown in section 4.5, we found that the main tunneling pathways for the anion coupling of butane-1,4-diyl were composed of a small number of pure h-transfer and pure e-transfer pathways. However, the sum of the couplings from these main tunneling pathways do not determine the entire T_{DA}-value. As shown in Fig. 4, when employing the Ruedenberg localization scheme with the 3-21G basis set for butane-1,4-diyl, the T_{DA}-value from eqn 16 with an energy threshold of 10^{-4} hartree was 9.239 mh, which was smaller than $T_{DA}=16.0$ mh calculated with an energy threshold of 10^{-9} hartree and from $\Delta/2=16.45$ mh calculated using eqn 2. Fig. 4 and 5 indicate that complicated interference effects among a large number of the minor tunneling pathways significantly contribute and as a result, the T_{DA}-value calculated with an energy threshold less than 10^{-7} hartree was in good agreement with $\Delta/2$. To examine the origin of a huge number of minor pathways and the interference effects among them, we have calculated the sum of the contributions from the intermediate states in CSF type X ($X=$ I − VI, see Fig. 2(c)) to the T_{DA}-value, as follows:

$$T_{DA}(X) = V_{DA}+\sum_{J\in X}\frac{V_{D,J}V_{J,A}}{E_{\rm tun}-E_J} + \sum_{J\in X}\sum_{K(\neq J)\in X}\frac{V_{D,J}V_{J,K}V_{K,A}}{(E_{\rm tun}-E_J)(E_{\rm tun}-E_K)}+\cdots. \quad (18)$$

Obviously, the above equation can be rewritten as eqn 16. Note that we took the sign of $T_{DA}({\rm All})$ positively and then determined the signs of the terms $T^{pth}_{DA}(X)$ in eqn 18 consistently.

In Table 7, we listed the results of $T^{pth}_{DA}(X)$'s, $T_{DA}(X)$'s, and the total number of pathways for the anion coupling of butane-1,4-diyl with the energy threshold of 10^{-9} hartree. In these calculations, the Ruedenberg localization scheme and the 3-21G basis set were used. The energy threshold and $E_{\rm tun}$ in eqn 18 were set to 10^{-9} and −91.9361747 (listed in Table 3) hartrees, respectively. We also listed the non-perturbative values $\Delta(X)/2$'s from eqn 2 where the CIs among $|\Phi_D\rangle$, $|\Phi_A\rangle$, and the intermediate states belonging to X were taken into account.

Table 7 shows that the $T_{DA}(X)$'s from eqn 18 were in reasonable agreement with the non-perturbative $\Delta(X)/2$'s from eqn 2, supporting the validity of the decomposition analyses using eqn 18 where up to 6th-order pathways contributions are taken into account. For $X=$ I and II, $T_{DA}(X)$'s were determined by $T^{2nd}_{DA}(X)+T^{3rd}_{DA}(X)$. These values can be explained by the contributions from the main tunneling pathways illustrated in Fig. 6. The $T^{2nd}_{DA}({\rm I+II})$ was in reasonable agreement with the $T^{2nd}_{DA}({\rm All})$, but the values of the other-order terms from $T^{3rd}_{DA}({\rm I+II})$ to $T^{6th}_{DA}({\rm I+II})$ were different from those of the corresponding terms for $X=$ All. The total number of pathways for $X=$ I + II was an order of magnitude smaller than that for $X=$ All. Since the main tunneling pathways were composed of pure h-transfer and pure e-transfer pathways involving the intermediate states in CSF types I and II, these differences indicate that the T_{DA}-value cannot be determined only by the contributions from the main tunneling pathways.

For $X=$ I + II + III, the $T^{2nd}_{DA}({\rm I+II+III})$ was almost identical with the $T^{2nd}_{DA}({\rm All})$. The $T^{3rd}_{DA}({\rm I+II+III})$ was in better agreement with the $T^{3rd}_{DA}({\rm All})$ than the $T^{3rd}_{DA}({\rm I+II})$. The additivity rule for the p-th order term, $T^{pth}_{DA}({\rm I+II+III}) = T^{pth}_{DA}({\rm I+II})+T^{pth}_{DA}({\rm III})$, was clearly not valid except for the second-order term. The additivity rules, $T^{pth}_{DA}({\rm I+III}) = T^{pth}_{DA}({\rm I})+T^{pth}_{DA}({\rm III})$ and $T^{pth}_{DA}({\rm II+III}) = T^{pth}_{DA}({\rm II})+T^{pth}_{DA}({\rm III})$, were also not valid except for the second-order terms. The total number of pathways for $X=$ I + II + III was much larger than the sum of the total pathways for $X=$ I + II and $X=$ III. These results indicate that the intermediate states in CSF type III produce a large number of the minor tunneling pathways involving the hybrid "electron/hole"-transfer via the interme-

Table 7 Decomposition of anion coupling of butane-1,4-diyl calculated at 3-21G level. For higher-order super-exchange calculations, the energy threshold of 10^{-9} hartree and Ruedenberg localization scheme were employed. The $\Delta(X)/2$ values were obtained from direct diagonalization of CIs

X	$T_{DA}^{\rm 2nd}(X)$ (mh)	$T_{DA}^{\rm 3rd}(X)$ (mh)	$T_{DA}^{\rm 4th}(X)$ (mh)	$T_{DA}^{\rm 5th}(X)$ (mh)	$T_{DA}^{\rm 6th}(X)$ (mh)	Number of pathways	$T_{DA}(X)$ (mh)	$\Delta(X)/2$ (mh)
I	5.30	3.68	0.0476	0.138	0.107	44073	6.69	13.3
II	6.51	−5.29	0.146	−0.212	0.0067	73511	−1.66	2.42
I+II	11.8	−2.08	0.225	−0.104	0.120	159472	7.40	8.96
III	1.02	−0.580	0.266	−0.110	0.0345	55692	1.96	1.67
I+III	6.32	2.72	7.46	1.19	0.00904	3133553	8.40	9.10
II+III	7.53	−9.17	5.64	−3.66	2.02	5593085	−0.231	0.862
I+II+III	12.8	−6.10	7.02	−2.82	2.51	9928058	10.9	9.02
I+II+III+VII	12.8	−6.67	9.94	−0.668	3.01	21134547	15.9	16.4
All	12.9	−7.00	10.3	−0.894	3.17	23581215	16.0	16.4

diate states in CSF types I and II together with those in CSF types III. Table 7 also shows that the intermediate states in CSF types IV significantly contribute to the the higher-order terms from $T_{DA}^{\rm 4th}$ to $T_{DA}^{\rm 6th}$ and increase the total number of pathways. These results suggest that the origin of a huge number of minor pathways is the hybrid e/h-transfer *via* the intermediate states in CSF types III and IV.

5 Comparison with NBO-based pathway analyses

5.1 Pathway analyses using the NBO Fock matrix

In many of the *ab initio*-MO based pathways-studies, the HF-KT scheme with NBOs[76,77] has been used.[12,17,18,50–57] However, the HF-KT scheme ignores the effects of non-dynamical electron correlation and orbital relaxation. While the errors arising from electron correlation and orbital relaxation in the T_{DA}-value tend to cancel each other for some ET systems[42], the errors arising in the tunneling pathways have been remained unclear. In contrast, our pathway analyses using the CI Hamiltonian matrix obtained from the localized MCSCF wave functions include both of the effects. Here, to clearly the significance of these effects, we compare the results from the ORMAS-MCSCF calculations with those from the HF-KT calculations with NBOs.

Curtiss *et al.*[39,50] have already conducted the pathway analyses for both the molecules in detail using the HF-KT scheme with NBOs. However, the structures used by Curtiss *et al.* were different from ours, which are shown in Fig. 1. We therefore reexamined the tunneling pathways with the NBO Fock matrix using our structures.

Employing the higher-order super-exchange method with the NBO Fock matrix, $\mathbf{F}^{\rm NBO}$, T_{DA} can be written by[18]

$$T_{DA} = F_{DA}^{\rm NBO} + \sum_j \frac{F_{D,j}^{\rm NBO} F_{j,A}^{\rm NBO}}{\varepsilon_{\rm tun} - \varepsilon_j^{\rm NBO}} + \sum_j \sum_{k(\neq j)} \frac{F_{D,j}^{\rm NBO} F_{j,k}^{\rm NBO} F_{j,k}^{\rm NBO}}{(\varepsilon_{\rm tun} - \varepsilon_j^{\rm NBO})(\varepsilon_{\rm tun} - \varepsilon_k^{\rm NBO})} + \cdots, \quad (19)$$

where $\varepsilon_j^{\rm NBO}$ and $F_{j,k}^{\rm NBO}$ are the diagonal and off-diagonal elements of the Fock matrix between the NBOs $\varphi_j^{\rm NBO}$ and $\varphi_k^{\rm NBO}$ and $\varepsilon_{\rm tun}$ is the tunneling energy used as a parameter. The donor and acceptor orbitals $\varphi_D^{\rm NBO}$ and $\varphi_A^{\rm NBO}$ are the NBOs corresponding to the lone-pair orbitals located on the terminal carbon atoms. Obviously, eqn 19 can be rewritten as eqn 16.

The NBOs were obtained by transforming the canonical β-spin (down-spin) UHF MOs solved for neutral triplets[39,52,54,55]. The tunneling energy was set to the self-energies of donor/acceptor NBOs (i.e., $\varepsilon_{\rm tun} = \varepsilon_D^{\rm NBO} = \varepsilon_A^{\rm NBO}$). We used the 3-21G and 6-31G(d) basis sets and took into account the contributions from up to 6th-order pathways to the T_{DA} values in eqn 19. We also calculated T_{DA} in the case that multiple visits to the bridge NBOs are prohibited in eqn 19. We always took the sign of T_{DA} obtained from eqn 19 positively and determined the signs of all of the β's and $T_{DA}^{p\rm th}$ consistently. Note that our sign convention used for T_{DA} is different from the previous studies.[50–55]

Table 8 summarizes the calculated results from eqn 19 with the energy threshold of 10^{-9} hartree. The $\Delta^{\rm UHF-KT}/2$ represents the half energy splitting between the two LUMOs for down-spin electron, listed in Tables 1 and 2. Table 8 shows that the $T_{DA}^{\rm 2nd}$ was remarkably larger than the other terms. The T_{DA}'s were in poor agreement with the $\Delta^{\rm UHF-KT}/2$ when multiple visits to the bridge NBOs were allowed. On the other hand, they were in reasonable agreement when multiple visits to the bridge NBOs were prohibited. Comparing Tables 5 and 6 with Table 8, the higher-order super-exchange calculations based on the localized MCSCF wave function can approximate the $\Delta/2$-values more effectively than those based on the HF-KT scheme with NBOs with only one exception (anion coupling of pentane-1,5-diyl at the 6-31G(d) level).

Fig. 7 illustrates the main tunneling pathways for anion coupling of butane-1,4-diyl using eqn 19 at the 3-21G level. As shown in Fig. 7, the main tunneling pathways consisted of a few number of pathways. Fig. 7(a) shows the second-order h-transfer pathway passing through the σ(C2-C3) NBO. Fig. 7(b) shows the second-order e-transfer pathway passing through the σ*(C2-C3) NBO. The couplings provided by these two pathways were remarkably large and almost reproduced the $T_{DA}^{\rm 2nd}$-value. Fig. 7(c) shows the main third-order tunneling pathway involving the Rydberg orbital at C1 or C4 atom. These main pathways have been already determined by Curtiss *et al.*[39], but the β-values provided by each of the pathways are different owing to the difference of the structure of the molecule. These main pathways partly correspond to

Table 8 Higher-order super-exchange calculations for anion couplings of butane-1,4-diyl and pentane-1,5-diyl using the NBO Fock matrix. The energy threshold of 10^{-9} hartree was employed

Molecule	Multiple visit	Basis Set	T_{DA}^{1st} (mh)	T_{DA}^{2nd} (mh)	T_{DA}^{3rd} (mh)	T_{DA}^{4th} (mh)	T_{DA}^{5th} (mh)	T_{DA}^{6th} (mh)	T_{DA} (mh)	$\frac{2\lvert T_{DA}\rvert}{\Delta^{UHF-KT}}$ (ratio)
butane	allowed	3-21G	−0.745	28.8	−1.43	−1.26	−0.599	−1.36	23.4	1.65
-1,4-diyl		6-31G(d)	−1.10	28.3	0.177	2.31	−6.97	3.05	25.8	2.43
	prohibited	3-21G	−0.745	28.8	−1.43	−7.51	−2.31	1.70	18.5	1.30
		6-31G(d)	−1.10	28.3	0.177	−8.83	−7.43	4.18	15.3	1.44
pentane	allowed	3-21G	0.0214	22.4	2.22	4.58	3.03	1.31	33.6	1.60
1,5-diyl		6-31G(d)	0.180	21.1	3.81	7.62	2.28	5.36	40.4	2.05
	prohibited	3-21G	0.0214	22.4	2.22	−10.8	−0.827	−0.506	22.3	1.05
		6-31G(d)	0.180	21.1	3.81	−0.417	−2.62	−1.05	21.0	1.07

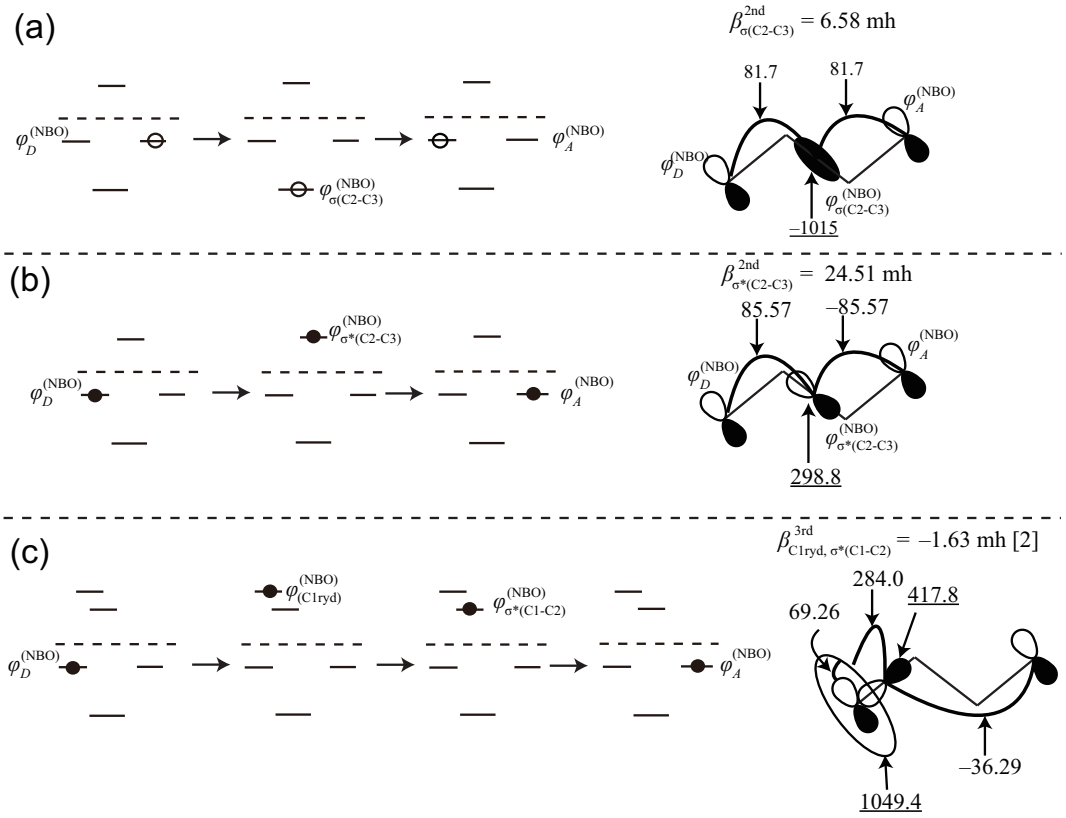

Fig. 7 Main tunneling pathways obtained from the super-exchange method with the NBO Fock matrix for anion coupling of butane-1,4-diyl. The 3-21G basis set was used. (a) The h-transfer pathway, (b) the e-transfer pathways, and (c) the third order pathways. The value of coupling β propagated by the corresponding pathway is given in millihartree (mh). The sign convention for the β-values is written in text. Matrix element $F^{NBO}_{j,k}$ and denominators ε^{NBO}_{j} (underlined) appeared in eqn 19 are also given in mh.

those obtained from the ORMAS-MCSCF calculations with the Ruedenberg scheme, illustrated in Fig. 6. However, the β-values provided by each of the main tunneling pathways in Fig. 6 are quite different from those in Fig. 7. The combined effect of non-dynamical correlation with orbital relaxation causes these differences.

5.2 Pathway analyses using CIs constructed from NBOs

Since the active orbitals are optimized in MCSCF calculations, our pathway analyses include the effect of orbital relaxation. To clarify this effect on the tunneling pathways, we now compare with the pathway analyses using the CI Hamiltonian matrix obtained from the frozen NBOs produced by HF calculation. Such pathway analyses are related to the work by Hayashi and Kato[58]. The anion coupling of butane-1,4-diyl was again dealt with at the 3-21G level.

Two sets of NBOs were used: one set obtained by transforming the canonical ROHF MOs solved for the neutral triplet diradical, and the other obtained by transforming the canonical ROHF MOs for the anion doublet radical. The obtained NBOs were divided into groups corresponding to those illustrated in Fig. 2 as follows: one group includes 4 carbon core NBOs, ORMAS group 1 includes eleven bonding and two lone pair NBOs, ORMAS group 2 includes eleven antibonding NBOs, and the other group includes the 24 Rydberg (extra-valence-shell) orbitals. The CIs were produced by the ORMAS setting described in section 3.2. From the ORMAS-CI calculation, we obtained 1872 CSFs corresponding to $|\Phi_D\rangle$ and $|\Phi_A\rangle$, and the six types CSFs illustrated in Fig. 2(b) and (c).

In the ORMAS-MCSCF calculations with orbital localization schemes described in Section 4, we always obtained the two Rydberg orbitals at C1 and C4 in ORMAS active group 2 as shown in Fig. 3. They contributed to the main tunneling pathways as shown in Fig. 6(b) and 6(c). Moreover, from the pathway analyses based on the NBO Fock matrix, the two Rydberg NBOs at C1 and C4 also contributed to the main tunneling pathways as shown in Fig. 7(c). Therefore, we have also conducted ORMAS-CI calculations by adding the Rydberg NBOs at C1 and C4 to the ORMAS active group 2. When using the 3-21G basis set, we obtained eight Rydberg NBOs at C1 and C4 and as a result, took into account 3224 CSFs in the ORMAS-CI calculations.

In Table 9, we listed the calculated values of the half energy splitting $\Delta^{\mathrm{ORMAS-CI}}/2$ between the ground and first excited states from the ORMAS-CI method with NBOs. Comparing Table 9 with Table 1, the $\Delta^{\mathrm{ORMAS-CI}}/2$-values involving the Rydberg orbitals at C1 and C4 were in reasonable agreement with the $\Delta/2$-values from the ORMAS-MCSCF calculations. These results indicate that the Rydberg orbitals at C1 and C4 are of great importance for the super-exchange anion coupling of butane-1,4-diyl.

In Table 9, we also summarize the results of higher-order super-exchange calculations using eqn 16. The E_{tun}-value in eqn 16 was taken from the converged values obtained from Löwdin projection-iteration calculations. The energy threshold of 10^{-9} hartree was used and up to 6th-order pathways were taken into account.

As shown in Table 9, the T_{DA}-values were in good agreement with the $\Delta^{\mathrm{ORMAS-CI}}/2$-values. We observed better convergence of the super-exchange calculations using the ORMAS-CIs with frozen NBOs against energy threshold than those using the ORMAS-MCSCF calculations with the orbital localization schemes. For example, the total number of pathways with the energy threshold of 10^{-9} hartree in the ORMAS-CIs with the NBOs solved for neutral triplet was 14075434 even if the eight Rydberg NBOs at C1 and C4 were included. This is much smaller than the total number of pathways in the ORMAS-MCSCF calculations with the Ruedenberg localization scheme shown in Table 7. This is related to the degree of localization of the reference orbitals constructing the CI Hamiltonian matrix. As shown in Fig. 3, the reference orbitals constructing the MCSCF wave function almost formed the desired localized orbitals, of which the shapes were similar to those of the NBOs. See Fig. S11, ESI.[†] Nevertheless, the orbitals in the localized MCSCF wave function involve the effects of orbital relaxation and the other extra-valence-shell orbitals that are not included in the ORMAS-CI calculations with the frozen NBOs. Thus, the reference orbitals constructing the localized MCSCF wave function were less localized than the frozen NBOs produced by the HF calculations.

Using eqn 18 with the CI Hamiltonian matrix constructed from the frozen NBOs, we decomposed the T_{DA} into the sum of contributions from the intermediate states in CSF type X. In Table 10, we listed $T_{DA}(X)$ and the total number of pathways calculated with the energy threshold of 10^{-9} hartree. We also listed the results of non-perturbative values $\Delta^{\mathrm{ORMAS-CI}}(X)/2$ where the CIs among $|\Phi_D\rangle$, $|\Phi_A\rangle$, and intermediate states in CSF type X were taken into account. Table 10 shows that the contributions from the pure e-transfer pathways were larger than those from pure h-transfer pathways in the ORMAS-CI calculations with the frozen NBOs, being opposite to the result from the ORMAS-MCSCF calculations (See Table 7). Taking into account the intermediate states in CSF type III in addition to those in CSF type I and II increased the total number of pathways by a factor of more than ten and brought the $T_{DA}(\mathrm{I+II+III})$-values closer to the $T_{DA}(\mathrm{All})$-values. Similarly to the result from the ORMAS-MCSCF calculations, the $T_{DA}(\mathrm{I+II+III+IV})$-values almost reproduced the $T_{DA}(\mathrm{All})$-values. In the ORMAS-MCSCF calculations, the contributions from the CSF type III and IV intermediate states were more prominent than those in the ORMAS-CI calculations with NBOs. However, the results in Tables 7 and 10 indicate that the intermediate states in CSF types III and IV produce a huge number of the hybrid "electron/hole"-transfer pathways and the interference effects among them significantly contribute to the T_{DA}-value, which does not depend much on the reference orbitals constructing CIs used for the pathway analyses.

6 Conclusion

In this paper, we have developed a method for the pathway analyses of super-exchange electronic couplings using the CI Hamiltonian matrix obtained from the localized ORMAS-MCSCF wave functions. Notable features of our method are as follows: (1) Both the effects of non-dynamical correlation and orbital relaxation are adequately taken into account. (2)

Table 9 Higher-order super-exchange calculations for anion coupling of butane-1,4-diyl using the CI Hamiltonian matrix constructed from the frozen NBOs. The 3-21G basis set and the energy threshold of 10^{-9} hartree were used

Reference orbitals	8 Rydberg orbitals at C1 and C4	T_{DA}^{1st} (mh)	T_{DA}^{2nd} (mh)	T_{DA}^{3rd} (mh)	T_{DA}^{4th} (mh)	T_{DA}^{5th} (mh)	T_{DA}^{6th} (mh)	T_{DA} (mh)	$\Delta^{ORMAS-CI}/2$ (ratio)
neutral triplet	none	0.449	18.4	2.18	3.24	1.45	1.16	26.8	22.59
	inclueded	0.449	11.4	0.0660	2.76	0.836	1.35	16.8	15.21
anion	none	−0.775	12.7	2.41	2.32	1.39	1.31	19.1	17.70
	inclueded	−0.775	12.3	1.97	2.35	1.34	1.01	18.2	16.98

Table 10 Decomposition of anion coupling of butane-1,4-diyl calculated using the CI Hamiltonian matrix constructed from the frozen NBOs including the Rydberg orbitals at C1 and C4 at the 3-21G level. For higher-order super-exchange calculations, the energy threshold of 10^{-9} hartree was employed. The $\Delta(X)/2$ values were obtained from direct diagonalization of CIs

Reference orbitals	X	$T_{DA}(X)$ (mh)	Number of pathways	$\Delta^{ORMAS-CI}(X)/2$ (mh)
neutral triplet	I	4.13	18821	7.57
	II	8.48	456885	8.34
	I+II	12.1	498870	11.5
	I+II+III	14.3	9270451	12.6
	I+II+III+VII	16.1	12852547	15.7
	All	16.8	14075434	15.2
anion	I	3.62	31411	5.73
	II	8.85	178706	10.8
	I+II	13.2	232960	15.6
	I+II+III	15.5	6912156	14.0
	I+II+III+VII	17.9	12009012	17.1
	All	18.2	13275446	17.0

Making use of the ORMAS method can provide accurate results with less computational efforts[107] and effectively produces the CSFs and the CI Hamiltonian matrix involving the tunneling pathways.

We applied our method to the anion couplings of butane-1,4-diyl and pentane-1,5-diyl. Using the Löwdin interaction-projection method, the converged values of $|H_{DA}^{eff}|$ from eqn 8 were in reasonable agreement with the $\Delta/2$-values from eqn 2, not depending on the basis sets and orbital localization schemes. Using the higher-order super-exchange method, the T_{DA}-values from eqn 15 were also in reasonable agreement with the $\Delta/2$-values. We found that the main tunneling pathways consist of a few number of lower-order pure h- and e-transfer pathways where σ(C-C), σ*(C-C), and extra-valence-shell (at the terminal carbon atoms) orbitals are used once or twice. Nevertheless, the T_{DA}-values cannot be explained solely by the main tunneling pathway contributions but the complicated interference effects among a huge number of the higher-order minor pathways significantly contribute to the T_{DA}-values, as shown in Fig. 4 and 5. Decomposition analyses using eqn 18 indicate that such a huge number of the higher-order pathways are attributed to the hybrid e/h-transfer pathways via the intermediate states in CSF types III and IV.

Comparing with the results from the HF-KT scheme with NBOs and the ORMAS-CI calculations with frozen NBOs, we have assessed the effects of non-dynamical correlation and orbital relaxation. The results are summarized as follows: (1) Both effects produce more than 1 mh differences in the $\Delta/2$-values except when the 3-21G basis set was employed (Tables 1 and 2). (2) Both effects produce remarkable differences in the β-values from each corresponding main pathways (Fig. 6 and 7). (3) The effect of the non-dynamical correlations produces a huge number of hybrid e/h-transfer pathways and complicates interference among them via the CSF type III and IV intermediate states (Fig. 4 and 5 and Tables 7 and 10). The HF-KT scheme with NBOs cannot give this insight for the pathway analysis. (4) The effect of orbital relaxation produces the obvious differences in the sum of the contributions from each intermediate CSF types (Tables 7 and 10). For instance, the contributions from the pure h-transfer pathways $T_{DA}(\mathrm{I})$ are larger than those from the pure e-transfer pathways $T_{DA}(\mathrm{II})$ in the ORMAS-MCSCF calculation, being opposite to the result from the ORMAS-CI calculation with frozen NBOs.

Since the feasibility of our MCSCF-based pathway analysis method is restricted by the number of CSFs, it remains to be improved for applications to large ET systems with respect to the following points: in this study the CI matrix elements H_{IJ} were first stored on the hard desk or core memory and then accessed for the subsequent pathway analysis. These demand huge storage capacities and computational times. Thus, it is desired to incorporate the pathway analysis algorithm directly into the ORMAS code for on-the-fly generation of H_{IJ}, and to calculate the decomposed values $\Delta(X)/2$ from eqn 2 with the Davidson method (*i.e.* not by standard diagonalization) in the manner of the direct CI. Moreover, the pathway analysis based on the super-exchange method (eqn 16) demands much computational cost to calculate and converge the higher-order terms. Thus, for large ET systems, the Löwdin method (eqn 8) and decompostion analyses $\Delta(X)/2$ are more adequate except for obtaining the main tunneling pathways.

For biological ET systems, the HF-KT analysis with NBOs and the tunneling current method are useful because the size of system is large and the relatively "coarse-grained" pathways are sufficient to determine the important parts of the protein

(for instance, amino acids level, main chain or side chain's contribution, the contributions from aromatic side chains, hydrogen bonds' importance, *etc.*) On the other hand, the DBA systems for molecular devices are relatively small and require highly accurate pathway analysis for molecular design. Therefore, our method will show much potential for the applications to these DBA systems.

7 Acknowledgment.

The authors acknowledge support from KAKENHI on Innovative Areas (No. 20108017, "π-space").

Notes and references

1 R. A. Marcus and N. Sutin, *Biochim. Biophys. Acta*, 1985, **811**, 265.
2 M. Bixon and J. Jortner, *Adv. Chem. Phys.*, 1999, **106**, 35.
3 A. M. Kuznetsov and J. Ulstrup, *ELECTRON TRANSFER IN CHEMICSTRY AND BIOLOGY, An introduction to the Theory*, Wiley, 1999.
4 D. DeVault, *Quantum Mechanical Tunneling in Biological Systems*, Cambridge University Press, 1984.
5 G. L. Closs, L. T. Calcaterra, N. J. Green, K. W. Penfield, and J. R. Miller, *J. Phys. Chem.*, 1986, **90**, 3673.
6 G. L. Closs and J. R. Miller, *Science*, 1988, **240**, 440.
7 M. D. Johnson, J. R. Miller, N. S. Green, and G. L. Closs, *J. Phys. Chem.*, 1989, **93**, 1173.
8 J. M. Warman, K. J. Smit, S. A. Jonker, J. W. Verhoeven, H. Oevering, J. Kroon, M. Paddon-Row, and A. M. Oliver, *Chem. Phys.*, 1993, **170**, 359.
9 M. Y. Ogawa, I. Moreira, J. F. Wishart, and S. S. Isied, *Chem. Phys.*, 1993, **176**, 589.
10 E. H. Yonemoto, G. B. Saupe, R. H. Schmehl, S. M. Hubig, R. L. Riley, B. L. Iverson, and T. E. Mallouk, *J. Am. Chem. Soc.*, 1994, **116**, 4786.
11 H. M. McConnell, *J. Chem. Phys.*, 1961, **35**, 508.
12 M. N. Paddon-Row, *Acc. Chem. Res.*, 1994, **27**, 18.
13 S. Larsson, *J. Am. Chem. Soc.*, 1981, **103**, 4034.
14 S. Larsson, *Chem. Soc.*, Faraday Trans. 2, 1983, **79**, 1375.
15 I. V. Kurnikov and D. N. Beratan, *J. Chem. Phys.*, 1996, **105**, 9561.
16 S. S Skourtis and D. N. Beratan, *Adv. Chem. Phys.*, 1999, **106**, 377.
17 M. D. Newton, *Chem. Rev.*, 1991, **91**, 767.
18 M. D. Newton and R. J. Cave, Molecular control of electron and hole transfer processes: electronic structure theory and application, in *Molecular Electronics, Chemistry for the 21st Century.*, ed. J. Jortner and M. A. Ratner, Blackwell, Malden, MA. **1997**, p. 73.
19 C.-P. Hsu, *Acc. Chem. Res.*, 2009, **42**, 509.
20 M. D. Newton, *Int. J. Quantum. Chem. Symp.*, 1980, **14**, 363.
21 K. Ohta, G. L. Closs, K. Morokuma, and N. J. Green, *J. Am. Chem. Soc.*, 1986, **108**, 1319.
22 M. D. Newton, *J. Phys. Chem.*, 1988, **92**, 3049.
23 A. Farazdel, M. Dupuis, E. Clementi, and A. Aviram, *J. Am. Chem. Soc.*, 1990, **112**, 4206.
24 A. Broo and S. Larsson, *Chem. Phys.*, 1990, **148**, 103.
25 K. Ando, *J. Chem. Phys.*, 1994, **101**, 2850.
26 L. Y. Zhang, R. A. Friesner, and R. B. Murphy, *J. Chem. Phys.*, 1997, **107**, 450.
27 S.-Z. Lu, X.-Y. Li, and J.-F. Liu, *J. Phys. Chem. A*, 2004, **108**, 4125.
28 J. F. Sanz and J. P. Malrieu, *J. Phys. Chem.*, 1993, **97**, 99.
29 R. J. Cave and M. D. Newton, *Chem. Phys. Lett.*, 1996, **249**, 15.
30 R. J. Cave and M. D. Newton, *J. Chem. Phys.*, 1997, **106**, 9213.
31 H.-C. Chen and C.-P. Hsu, *J. Phys. Chem. A*, 2005, **109**, 11989.
32 J. Subotnik, S. Yeganeh, R. J. Cave, and M. A. Ratner, *J. Chem. Phys.*, 2008, **129**, 244101.
33 A. A. Voityuk and N. Rösch, *J. Chem. Phys.*, 2002, **117**, 5607.
34 Q. Wu and T. V. Voorhis, *J. Chem. Phys.*, 2006, **125**, 164105.
35 A. Migliore, *J. Chem. Phys.*, 2009, **131**, 114113.
36 A. A. Stuchebrukhov, *Adv. Chem. Phys.*, 2001, **118**, 1.
37 A. A. Stuchebrukhov, *Theor. Chem. Acc.*, 2003, **110**, 291.
38 K. D. Jordan and M. N. Paddon-Row, *J. Phys. Chem.*, 1992, **96**, 1188.
39 L. A. Curtiss, C. A. Naleway, and J. R. Miller, *J. Phys. Chem.*, 1993, **97**, 4050.
40 L. Rodriguez-Monge and S. Larsson, *J. Phys. Chem.*, 1996, **100**, 6298.
41 K. Kim, K. D. Jordan, and M. N. Paddon-Row, *J. Phys. Chem.*, 1994, **98**, 11053.
42 L. A. Curtiss, and J. R. Miller, *J. Phys. Chem. A*, 1998, **102**, 160.
43 L. Rodriguez-Monge and S. Larsson, *Int. J. Quant. Chem.*, 1997, **61**, 847.
44 E. Cukier and R. J. Cave, *Chem. Phys. Lett.*, 2005, **402**, 186.
45 Z.-Q. You, Y. Shao, and C.-P. Hsu, *Chem. Phys. Lett.*, 2004, **390**, 116.
46 C.-H. Yang and C.-P. Hsu, *J. Chem. Phys.*, 2006, **124**, 244507.
47 T. R. Prytkova, I. V. Kurnikov, and D. N. Beratan, *J. Phys. Chem. B*, 2005, **109**, 1618.
48 M. R. Hartings, I. V. Kurnikov, A. R. Dunn, J. R. Winker, H. B. Gray, and M. A. Ratner, *Coord. Chem. Rev.*, 2010, **254**, 248
49 M. A. Ratner, *J. Phys. Chem.*, 1990, **94**, 4877.
50 C. A. Naleway, L. A. Curtiss, and J. R. Miller, *J. Phys. Chem.*, 1991, **95**, 8434.
51 L. A. Curtiss, C. A. Naleway, and J. R. Miller, *Chem. Phys.*, 1993, **176**, 387.
52 L. A. Curtiss, C. A. Naleway, and J. R. Miller, *J. Phys. Chem.*, 1995, **99**, 1182.
53 P. P. Paulson, L. A. Curtiss, B. Bal, G. L. Closs, and J. R. Miller, *J. Am. Chem. Soc.*, 1996, **118**, 378.
54 C. Liang and M. D. Newton, *J. Phys. Chem.*, 1992, **96**, 2855.

55 C. Liang and M. D. Newton, *J. Phys. Chem.*, 1993, **97**, 3199.
56 K. D. Jordan and M. N. Paddon-Row, *Chem. Rev.*, 1992, **92**, 395.
57 M. J. Shephard, M. N. Paddon-Row, and K. D. Jordan, *J. Am. Chem. Soc.*, 1994, **116**, 5328.
58 S. Hayashi and S. Kato, *J. Phys. Chem. A*, 1998, **102**, 2878.
59 C. C. Moser, J. M. Keske, K. Warnucke, R. S. Farid, and P. L. Dutton, *Nature*, 1992, **355**, 796.
60 C. C. Page, C. C. Moser, X. Chen, and P. L. Dutton, *Nature*, 1999, **402**, 47.
61 D. N. Beratan, J. N. Onuchic, and J. J. Hopfield, *J. Chem. Phys.*, 1987, **86**, 4488.
62 D. N. Beratan, J. N. Betts, and J. N. Onuchic, *Science*, 1991, **252**, 1285.
63 D. N. Beratan, J. N. Betts, and J. N. Onuchic, *J. Phys. Chem.*, 1992, **96**, 2852.
64 J. J. Regan and J. N. Onuchic, *Adv. Chem. Phys.*, 1999, **107**, 497.
65 S. S Skourtis and D. N. Beratan, *J. Phys. Chem. B*, 1997, **101**, 1215.
66 J. R. Winkler, *Cur. Op. Chem. Biol.*, 2000, **4**, 192.
67 T. Kawatsu, T. Kakitani, and T. Yamato, *Inorg. Chim. Acta*, 2000, **300-302**, 862.
68 T. Kawatsu, T. Kakitani, and T. Yamato, *J. Phys. Chem. B*, 2001, **105**, 4424.
69 H. Nishioka, A. Kimura, T. Yamato, T. Kawatsu, and T. Kakitani, *J. Phys. Chem. B*, 2005, **109**, 1078.
70 Y. Miyazawa, H. Nishioka, K. Yura, and T. Yamato, *Biophys. J.*, 2008, **94**, 2194.
71 T. Kawatsu, D. N. Beratan, and T. Kakitani, *J. Phys. Chem. B*, 2006, **110**, 5747.
72 H. Nishioka and T. Kakitani, *J. Phys. Chem. B*, 2008, **112**, 9948.
73 A. A. Stuchebrukhov, *J. Chem. Phys.*, 1996, **105**, 10819.
74 X. Zheng and A. A. Stuchebrukhov, *J. Phys. Chem. B*, 2003, **107**, 6621.
75 X. Zheng and A. A. Stuchebrukhov, *J. Phys. Chem. B*, 2003, **107**, 9579.
76 J. P. Foster and F. Weinhold, *J. Am. Chem. Soc.*, 1980, **102**, 7211.
77 A. E. Reed, R. B. Weinstock, and F. Weinhold, *J. Chem. Phys.*, 1985, **83**, 735.
78 J. Ivanic, *J. Chem. Phys.*, 2003, **119**, 9364.
79 M. W. Schmidt, K. K. Baldridge, J. A. Boatz, S. T. Elbert, M. S. Gordon, J. H. Jensen, S. Koseki, N. Matsunaga, K. A. Nguyen, S. J. Su, T. L. Windus, M. Dupuis, and J. A. Montgomery, *J. Comput. Chem.*, 1993, **14**, 1347.
80 C. Edmiston and K. Ruedenberg, *Rev. Mod. Phys.*, 1963, **35**, 457.
81 S. F. Boys, *Quantum Science of Atoms, Molecules, and Solids* P. O. Löwdin, Ed, Academic Press, NY, 1966, pp 253-262.
82 J. Pipek and P. Z. Mezey, *J. Chem. Phys.*, 1989, **90**, 4916.
83 P. O. Löwdin, *J. Math. Phys.*, 1962, **3**, 969.
84 P. O. Löwdin, *J. Mol. Spectosc.*, 1964, **13**, 326.
85 C. E. D. Chidsey, *Science*, 1991, **251**, 919.
86 C. Miller, P. Cuendet, and M. Grätzel, *J. Phys. Chem.*, 1991, **95**, 877.
87 H. O. Finklea and D. D. Hanshew, *J. Am. Chem. Soc.*, 1992, **114**, 3173.
88 D. N. Beratan, S. S. Skourtis, I. A. Balabin, A. Balaeff, S. Keinan, R. Venkatramani, and D. Xiao, *Acc. Chem. Res.*, 2009, **42**, 1669.
89 S. S. Skourtis, D. H. Waldeck, and D. N. Beratan, *Annu. Rev. Chem.*, 2010, **61**, 461.
90 A. D. Becke, *J. Chem. Phys.*, 1993, **98**, 5648.
91 We used FCCIHE routine contained in ORMAS1 routine in the GAMESS[79] program to calculate the the CI Hamiltonian matrix elements in a direct manner by use of the Slater-Condon rule.
92 T. Helgaker, P. Jorgensen, and J. Olsen, *Molecular Electronic-Structure Theory*, 2000, Wiley, Chichester.
93 P. C. P. de Andrade and J. A. Freire, *J. Chem. Phys.*, 2004, **120**, 7811.
94 S. Priyadarshy, S. S. Skourtis, S. M. Risser, and D. N. Beratan, *J. Chem. Phys.*, 1996, **104**, 9473.
95 O. L. de Santana and A. A. S. da Gama, *Chem. Phys. Lett.*, 1999, **314**, 508.
96 A. Teklos and S. S. Skourtis, *J. Chem. Phys.*, 2006, **125**, 244103.
97 S. S. Skourtis, D. N. Beratan, and J. N. Onuchic, *Chem. Phys.*, 1993, **176**, 501.
98 W. J. Hehre, R. F. Stewart, and J. A. Pople, *J. Chem. Phys.*, 1969, **51**, 2657.
99 J. S. Binkley and J. A. Pople, *J. Am. Chem. Soc.*, 1980, **102**, 939.
100 W. J. Hehre, R. Ditchfield, and J. A. Pople, *J. Chem. Phys.*, 1972, **56**, 2257.
101 R. Krishnan, J. S. Binkley, R. Seeger, and J. A. Pople, *J. Chem. Phys.*, 1980, **72**, 650.
102 M. M. Francl, W. J. Pietro, W. J. Hehre, J. S. Binkley, M. S. Gordon, D. J. DeFrees, and J. A. Pople, *J. Chem. Phys.*, 1982, **77**, 3654.
103 T. H. Jr. Dunning, *J. Chem. Phys.*, 1989, **90**, 1007.
104 M. J. Frisch, J. A. Pople, and J. S. Binkley, *J. Chem. Phys.*, 1984, **80**, 3265.
105 J. A. Nobel, S. B. Trickey, J. R. Sabin, and J. Oddershede, *Chem. Phys.*, 2005, **309**, 89.
106 C. Herrmann, G. C. Solomon, J. E. Subotnik, V. Mujica, and M. A. Ratner, *J. Chem. Phys.*, 2010, **132**, 24103.
107 J. Ivanic, *J. Chem. Phys.*, 2003, **119**, 9377.
108 Winmostar Web site; http://winmostar.com/